ARMY RESEARCH LABORATORY

Cantilever Beam Design for Projectile Internal Moving Mass Systems

by Jonathan Rogers and Mark Costello

ARL-CR-658 **September 2010**

prepared by

Georgia Institute of Technology
School of Aerospace Engineering
Atlanta, GA 30332

under contract

W911QX-06-C-0013

NOTICES

Disclaimers

The findings in this report are not to be construed as an official Department of the Army position unless so designated by other authorized documents.

Citation of manufacturer's or trade names does not constitute an official endorsement or approval of the use thereof.

Destroy this report when it is no longer needed. Do not return it to the originator.

Army Research Laboratory
Aberdeen Proving Ground, MD 21005-5066

ARL-CR-658 **September 2010**

Cantilever Beam Design for Projectile Internal Moving Mass Systems

Jonathan Rogers and Mark Costello
Georgia Institute of Technology

prepared by

Georgia Institute of Technology
School of Aerospace Engineering
Atlanta, GA 30332

under contract

W911QX-06-C-0013

REPORT DOCUMENTATION PAGE	Form Approved OMB No. 0704-0188

1. REPORT DATE *(DD-MM-YYYY)*	2. REPORT TYPE	3. DATES COVERED (From - To)
September 2010	Final	September 2007–May 2010

4. TITLE AND SUBTITLE
Cantilever Beam Design for Projectile Internal Moving Mass Systems

5a. CONTRACT NUMBER
W911QX-06-C-0013

5b. GRANT NUMBER

5c. PROGRAM ELEMENT NUMBER

6. AUTHOR(S)
Jonathan Rogers* and Mark Costello*

5d. PROJECT NUMBER
AH80

5e. TASK NUMBER

5f. WORK UNIT NUMBER

7. PERFORMING ORGANIZATION NAME(S) AND ADDRESS(ES)
School of Aerospace Engineering
Georgia Institute of Technology
Atlanta, GA 30332

8. PERFORMING ORGANIZATION REPORT NUMBER

9. SPONSORING/MONITORING AGENCY NAME(S) AND ADDRESS(ES)
U.S. Army Research Laboratory
ATTN: RDRL-WMB-C
Aberdeen Proving Ground, MD 21005-5066

10. SPONSOR/MONITOR'S ACRONYM(S)
ARL

11. SPONSOR/MONITOR'S REPORT NUMBER(S)
ARL-CR-658

12. DISTRIBUTION/AVAILABILITY STATEMENT
Approved for public release; distribution is unlimited.

13. SUPPLEMENTARY NOTES
* School of Aerospace Engineering, Georgia Institute of Technology, Atlanta, GA 30332

14. ABSTRACT

Internal masses that undergo controlled translation within a projectile have been shown to be effective control mechanisms for smart weapons. However, internal mass oscillation must occur at the projectile roll frequency to generate sufficient control force. This can lead to high power requirements and place a heavy burden on designers attempting to allocate volume within the projectile for internal mass actuators and power supplies. The work reported here outlines a conceptual design for an internal translating mass system using a cantilever beam and electromagnetic actuators. The cantilever beam acts as the moving mass, vibrating at the projectile roll frequency to generate control force. First, a dynamic model is developed to describe the system. Then, the natural frequency, damping ratio, and length of the beam are varied to study their effects on force required and total battery size. Trade studies also examine the effect on force required and total battery size of a roll-rate feedback system that actively changes beam elastic properties. Results show that with proper sizing and specifications, the cantilever beam control mechanism requires relatively small batteries and low actuator control forces, with minimum actuator complexity and space requirements.

15. SUBJECT TERMS
internal translating mass, ITM, smart weapons, cantilever beam

16. SECURITY CLASSIFICATION OF:			17. LIMITATION OF ABSTRACT	18. NUMBER OF PAGES	19a. NAME OF RESPONSIBLE PERSON
a. REPORT	b. ABSTRACT	c. THIS PAGE			Paul Weinacht
Unclassified	Unclassified	Unclassified	UU	48	19b. TELEPHONE NUMBER (*Include area code*) 410-306-0800

Standard Form 298 (Rev. 8/98)
Prescribed by ANSI Std. Z39.18

Table of Contents

List of Figures **iv**

List of Tables **v**

1. Introduction **1**

2. Cantilever Beam Projectile Dynamic Model **2**

2.1 Kinematics....4

2.2 Dynamics....5

2.3 Description of Controller....7

2.4 Description of Electromagnetic Actuator Control System....8

2.5 Description of Example Projectile....9

3. Results **10**

4. Conclusion **23**

5. References **25**

Appendix A. *A* and *B* Matrix Terms **27**

Appendix B. Translating Mass Projectile Schematic **31**

List of Symbols, Abbreviations, and Acronyms **33**

Distribution List **36**

List of Figures

Figure 1. The ITM-Beam projectile. 2
Figure 2. Zoom view of the ITM-Beam system. 8
Figure 3. Altitude vs. range for example trajectory. 10
Figure 4. Cross range vs. range for example trajectory. 11
Figure 5. Velocity (u) vs. time for example trajectory. 11
Figure 6. Roll rate vs. time for example trajectory. The thick lines represent high-frequency oscillations, which occur only for the ITM-Beam and translating mass case. 12
Figure 7. Selected time history of ITM displacement from projectile centerline. 13
Figure 8. Segment of current vs. time for ITM-Beam actuators. 14
Figure 9. Maximum angular displacement vs. beam length. 15
Figure 10. Average force required vs. beam length. 15
Figure 11. Roll rate vs. time for example simulation. 16
Figure 12. Average force required vs. torsional spring constant, partial flight profile. 17
Figure 13. Average power required vs. torsional spring constant, partial flight profile. 18
Figure 14. Total charge required vs. torsional spring constant, partial flight profile. 18
Figure 15. Average force required vs. torsional spring constant, full flight profile. 19
Figure 16. Average power required vs. torsional spring constant, full flight profile. 19
Figure 17. Total charge required vs. torsional spring constant, full flight profile. 20
Figure 18. Current through actuators vs. time for example full flight trajectory 21
Figure 19. Torsional spring constant vs. time for roll-rate feedback system, $\zeta = 0.05$. 22
Figure 20. Total charge required vs. damping ratio for constant and variable k_T cases. 23
Figure B-1. Translating mass projectile schematic. 32

List of Tables

Table 1. Relevant example projectile and ITM-Beam properties. 9
Table 2. Performance evaluation of roll-rate feedback system. 23

INTENTIONALLY LEFT BLANK.

1. Introduction

The past several decades have seen growing interest in developing of smart munitions resulting from attempts to increase accuracy and decrease collateral damage. Smart projectiles differ from other guided weapons, such as guided missiles, because their electronics and control mechanisms must be able to withstand extreme acceleration loads associated with launch and high spin rates. Control components must be relatively inexpensive since projectiles are typically fired in large quantities. Several different types of control mechanisms have been designed to meet these requirements—aerodynamic, thrust, and inertial load mechanisms. Common examples of aerodynamic mechanisms are canards, gimbaled nose configurations, and deflection of ram air through side ports. Examples of thrust mechanisms include cold gas jets and explosive thrusters. Examples of inertial load mechanisms are rotation of an unbalanced internal part and, of specific interest here, movement of an internal translating mass (ITM). Oscillation of an internal mass at the projectile roll frequency has been shown to produce useful control authority. A design that minimizes moving parts and substantially reduces power required is critical to physically implement an ITM control mechanism on board a smart munition.

Previous investigation of projectiles equipped with loose or moving internal parts has revealed that these configurations can result in flight instabilities. Soper (*1*) considered the stability of a projectile with a cylindrical mass fitted loosely within a cavity. Using a similar configuration, Murphy (*2*) derived a quasi-linear solution for the motion of a projectile equipped with a moving internal part. A detailed set of experiments was later conducted by D'Amico (*3*) to model the motion of internal masses within spinning projectiles using a freely gimbaled gyroscope. Hodapp (*4*) further considered the effect of a small offset between the projectile body mass and ITM mass center. Hodapp's analysis of the dynamic equations for this system showed that for small mass center offsets, slight movement could actually reduce the instability caused by the loose internal part. Using controlled movement of an ITM as a maneuver control mechanism was considered by Petsopoulous et al. (*5*) for use on re-entry vehicles, while Robinett et al. (*6*) considered ITM control for ballistic rockets. More recently, Menon et al. (*7*) examined ITM control for use on endo- and exoatmospheric interceptors using three orthogonal ITMs. Frost and Costello (*8, 9*) have studied the ability of an internal rotating mass unbalance to actively control both fin- and spin-stabilized projectiles. Most recently, Rogers and Costello (*10*) investigated control authority of a projectile equipped with a single internal translating mass. It was determined that significant control authority could be created by oscillating the ITM at the projectile roll frequency.

This report outlines a notional design of an ITM actuator that generates sufficient control authority using relatively low power. Control moment is generated due to an axial drag offset from the system mass center caused by the lateral motion of the ITM. The report begins with a description of the cantilever beam system that serves as the translating mass and derives the 7-degrees-of-freedom (DOF) flight dynamic model used for trajectory predictions. A description of the control law and ITM electromagnetic actuators is also provided. The dynamic model is subsequently employed to demonstrate that the cantilever beam configuration provides sufficient control authority at reasonable power levels. Trade studies examine the effect of cantilever beam length on force required and battery size. The optimum natural frequency and damping ratio of the beam are determined to minimize actuator control effort. Finally, roll-rate feedback control is implemented to actively alter beam characteristics as the projectile roll rate changes during flight, further decreasing control effort required. A final example case demonstrates that sufficient control authority can be generated with relatively small battery sizes using the optimum spring and damper coefficients and the roll-rate feedback system.

2. Cantilever Beam Projectile Dynamic Model

The cantilever beam is a fixed-free elastic beam, with one end attached to the projectile at point L and the free end floating within the cavity, constrained to vibrate in the $\vec{I}_s - \vec{J}_s$ plane. The beam's first vibrational mode is the only mode considered significant to dynamic interaction with the projectile. For this reason, the cantilever beam can be accurately modeled as a rigid, massless beam, with a spherical mass (considered to be a permanent magnet) attached to the end. A torsional spring and damper are attached to the hinge point to simulate the elastic properties of the cantilever beam. This dynamically equivalent system is referred to as the ITM-Beam. A sketch of this configuration is shown in figure 1. Note that γ is defined as the angle between the ITM-Beam and centerline of the projectile. A permanent magnet is attached to the end of the beam and can swing freely about the hinge. Force is exerted on the magnet by electromagnets on both sides of the cavity to move the beam to a desired angle.

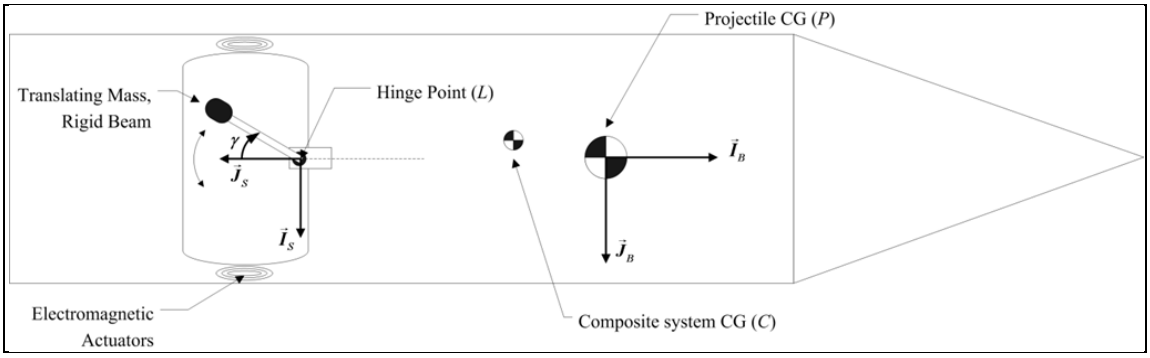

Figure 1. The ITM-Beam projectile.

Five reference frames are used in the development of the equations of motion for this system, namely the inertial, projectile, translating mass, nonrolling, and projectile-fixed *S* reference frames. The projectile frame is obtained using the standard aerospace Euler angle sequence of rotations and is related to the inertial frame by

$$\begin{Bmatrix} \vec{I}_B \\ \vec{J}_B \\ \vec{K}_B \end{Bmatrix} = \begin{bmatrix} c_\theta c_\psi & c_\theta s_\psi & -s_\theta \\ s_\phi s_\theta c_\psi - c_\phi s_\psi & s_\phi s_\theta s_\psi + c_\phi c_\psi & s_\phi c_\theta \\ c_\phi s_\theta c_\psi + s_\phi s_\psi & c_\phi s_\theta s_\psi - s_\phi c_\psi & c_\phi c_\theta \end{bmatrix} \begin{Bmatrix} \vec{I}_I \\ \vec{J}_I \\ \vec{K}_I \end{Bmatrix} . \tag{1}$$

The *N* frame is the standard nonrolling reference frame often used in projectile flight dynamics and is defined by a rotation of $-\phi$ along the $\vec{I}_B$ axis. The *S* frame is also fixed to the projectile, with its origin at the hinge point. It is defined so that the ITM-Beam oscillates about the $\vec{K}_S$ axis and $\vec{J}_S$ points to the rear of the cavity exactly equidistant from both electromagnetic actuators. Therefore, the *S* frame can be related to the *B* frame by two constant Euler angles, ψ_S and θ_S, so that

$$\begin{Bmatrix} \vec{I}_S \\ \vec{J}_S \\ \vec{K}_S \end{Bmatrix} = \begin{bmatrix} c_{\theta_S} c_{\psi_S} & c_{\theta_S} s_{\psi_S} & -s_{\theta_S} \\ -s_{\psi_S} & c_{\psi_S} & 0 \\ s_{\theta_S} c_{\psi_S} & s_{\theta_S} s_{\psi_S} & c_{\theta_S} \end{bmatrix} \begin{Bmatrix} \vec{I}_B \\ \vec{J}_B \\ \vec{K}_B \end{Bmatrix} . \tag{2}$$

Throughout the rest of this report, fixed angles of $\psi_S = 90°$ and $\theta_S = 0$ are used; thus, the *S* frame can be obtained by a single 90° rotation about the $\vec{K}_B$ axis, resulting in the orientation shown in figure 1. The *T* frame is fixed to the ITM-Beam and is related to the *S* frame by the relationship

$$\begin{Bmatrix} \vec{I}_T \\ \vec{J}_T \\ \vec{K}_T \end{Bmatrix} = \begin{bmatrix} c_\gamma & s_\gamma & 0 \\ -s_\gamma & c_\gamma & 0 \\ 0 & 0 & 1 \end{bmatrix} \begin{Bmatrix} \vec{I}_S \\ \vec{J}_S \\ \vec{K}_S \end{Bmatrix} . \tag{3}$$

Note that the *T* frame is aligned with the *S* frame when $\gamma = 0$. All equations in this report use the following shorthand notation for trigonometric sine, cosine, and tangent functions: $s_\alpha = \sin\alpha$, $c_\alpha = \cos\alpha$, and $t_\alpha = \tan\alpha$.

Throughout the development of the equations of motion, two operators will be used: $\mathbb{C}$ to denote components of a vector in a specific frame and $\mathbb{S}$ to denote the skew symmetric cross product operator. The vector component operator outputs a column vector comprised of the components of an input vector in a given frame. For example, if the position vector from α to β is expressed in reference frame A as $\vec{r}_{\alpha\to\beta} = \Delta x_{\alpha\beta}\vec{I}_A + \Delta y_{\alpha\beta}\vec{J}_A + \Delta z_{\alpha\beta}\vec{K}_A$, then the vector component operator acting on this vector yields

$$\mathbb{C}_A(\vec{r}_{\alpha\to\beta}) = \begin{Bmatrix} \Delta x_{\alpha\beta} \\ \Delta y_{\alpha\beta} \\ \Delta z_{\alpha\beta} \end{Bmatrix} . \tag{4}$$

Notice that the reference frame is denoted by the subscript on the operator.

The cross-product operator outputs a skew symmetric matrix using the components of an input vector in the reference frame denoted in the subscript. For example, if the position vector from α to β is expressed in reference frame A as $\vec{r}_{\alpha\to\beta} = \Delta x_{\alpha\beta}\vec{I}_A + \Delta y_{\alpha\beta}\vec{J}_A + \Delta z_{\alpha\beta}\vec{K}_A$, then the cross-product operator acting on $\vec{r}_{\alpha\to\beta}$ expressed in reference frame A is

$$\mathbb{S}_A(\vec{r}_{\alpha\to\beta}) = \begin{bmatrix} 0 & -\Delta z_{\alpha\beta} & \Delta y_{\alpha\beta} \\ \Delta z_{\alpha\beta} & 0 & -\Delta x_{\alpha\beta} \\ -\Delta y_{\alpha\beta} & \Delta x_{\alpha\beta} & 0 \end{bmatrix} . \tag{5}$$

2.1 Kinematics

The velocity of the composite body mass center can be described in the inertial frame or the projectile reference frame.

$$\vec{v}_{C/I} = \dot{x}\vec{I}_I + \dot{y}\vec{J}_I + \dot{z}\vec{K}_I = u\vec{I}_B + v\vec{J}_B + w\vec{K}_B \ . \tag{6}$$

The translational kinematic differential equations relate these two representations of the mass center velocity components.

$$\begin{Bmatrix} \dot{x} \\ \dot{y} \\ \dot{z} \end{Bmatrix} = \begin{bmatrix} c_\theta c_\psi & s_\phi s_\theta c_\psi - c_\phi s_\psi & c_\phi s_\theta c_\psi + s_\phi s_\psi \\ c_\theta s_\psi & s_\phi s_\theta s_\psi + c_\phi c_\psi & c_\phi s_\theta s_\psi - s_\phi c_\psi \\ -s_\theta & s_\phi c_\theta & c_\phi c_\theta \end{bmatrix} \begin{Bmatrix} u \\ v \\ w \end{Bmatrix} . \tag{7}$$

The angular velocity of the projectile with respect to the inertial reference frame can be written in terms of appropriate Euler angle time derivatives or in terms of projectile frame angular velocity components.

$$\vec{\omega}_{B/I} = \dot{\phi}\vec{I}_B + \dot{\theta}\vec{J}_N + \dot{\psi}\vec{K}_I = p\vec{I}_B + q\vec{J}_B + r\vec{K}_B \ . \tag{8}$$

The kinematic relationship between time derivatives of the Euler angles and projectile reference frame angular velocity components represents the rotational kinematic differential equations.

$$\begin{Bmatrix} \dot{\phi} \\ \dot{\theta} \\ \dot{\psi} \end{Bmatrix} = \begin{bmatrix} 1 & s_\phi t_\theta & c_\phi t_\theta \\ 0 & c_\phi & -s_\phi \\ 0 & s_\phi / c_\theta & c_\phi / c_\theta \end{bmatrix} \begin{Bmatrix} p \\ q \\ r \end{Bmatrix} . \tag{9}$$

The final kinematic differential equation is the trivial relationship

$$\dot{\gamma} = \omega_{Beam} \ . \tag{10}$$

2.2 Dynamics

The translational dynamic equations for the ITM-Beam projectile are derived through force balancing. Force-balance equations for the projectile and ITM-Beam are given as

$$\boldsymbol{m_P}\vec{\boldsymbol{a}}_{\boldsymbol{P/I}} = \vec{\boldsymbol{W}}_{\boldsymbol{P}} + \vec{\boldsymbol{F}}_{\boldsymbol{P}} - \vec{\boldsymbol{F}}_{\boldsymbol{C}} - \vec{\boldsymbol{F}}_{\boldsymbol{I}} \tag{11}$$

and

$$\boldsymbol{m_T}\vec{\boldsymbol{a}}_{\boldsymbol{X/I}} = \vec{\boldsymbol{W}}_{\boldsymbol{T}} + \vec{\boldsymbol{F}}_{\boldsymbol{C}} + \vec{\boldsymbol{F}}_{\boldsymbol{I}}, \tag{12}$$

respectively, where $\boldsymbol{m}_P$ and $\boldsymbol{m}_T$ are the masses of the projectile and ITM-Beam, $\vec{\boldsymbol{a}}_{P/I}$ and $\vec{\boldsymbol{a}}_{X/I}$ are the accelerations of points *P* and *X* with respect to the inertial frame, and $\vec{\boldsymbol{W}}_P$, $\vec{\boldsymbol{W}}_T$, $\vec{\boldsymbol{F}}_P$, $\vec{\boldsymbol{F}}_I$ and $\vec{\boldsymbol{F}}_C$ are the weights of the projectile and ITM-Beam, total aerodynamic force exerted on the projectile, input force exerted on the ITM-Beam by the actuators, and hinge constraint force, respectively. The definition of the system center of mass leads to

$$\boldsymbol{m}\vec{\boldsymbol{a}}_{\boldsymbol{C/I}} = \boldsymbol{m_P}\vec{\boldsymbol{a}}_{\boldsymbol{P/I}} + \boldsymbol{m_T}\vec{\boldsymbol{a}}_{\boldsymbol{X/I}} \ . \tag{13}$$

Therefore, adding equations 11 and 12 and noting the relationship in equation 13, the translational dynamic equation for the system is formed.

$$\boldsymbol{m}\vec{\boldsymbol{a}}_{\boldsymbol{C/I}} = \vec{\boldsymbol{W}}_{\boldsymbol{P}} + \vec{\boldsymbol{W}}_{\boldsymbol{T}} + \vec{\boldsymbol{F}}_{\boldsymbol{P}} \ . \tag{14}$$

The aerodynamic forces given by $\vec{\boldsymbol{F}}_P$ in equation 14 are obtained using the standard aerodynamic expansion employed for projectile flight dynamic simulation. Both steady aerodynamic forces and Magnus forces are included as well as steady and unsteady aerodynamic moments. The aerodynamic coefficients and aerodynamic center distances used to generate these forces and moments are all a function of the local Mach number at the center of mass of the projectile. Computationally, these Mach number-dependent parameters are obtained by a table look-up scheme using linear interpolation. A full description of the weight force and body aerodynamic forces and moments is provided in reference *10*. Writing equation 14 in the projectile reference frame yields

$$\begin{Bmatrix} \dot{u} \\ \dot{v} \\ \dot{w} \end{Bmatrix} = \begin{Bmatrix} \frac{X_B}{m} \\ \frac{Y_B}{m} \\ \frac{Z_B}{m} \end{Bmatrix} - \begin{bmatrix} 0 & -r & q \\ r & 0 & -p \\ -q & p & 0 \end{bmatrix} \begin{Bmatrix} u \\ v \\ w \end{Bmatrix} \ . \tag{15}$$

Note that X_B, Y_B, and Z_B are projectile reference frame components of the sum of the three forces given in equation 14.

The rotational dynamic equations are obtained by first equating the I frame time rate of change of the system angular momentum about the system mass center to the total applied external moments on the system about the system mass center in the $\vec{I}_S$ and $\vec{J}_S$ directions, given by equations 16 and 17. Then, the same moment equation is used for each body separately, this time written in the $\vec{K}_S$ direction. These four equations are given by

$$\vec{I}_S \bullet \left(\frac{{}^I d\vec{H}^P_{B/I}}{dt} + \frac{{}^I d\vec{H}^X_{T/I}}{dt} + \vec{r}_{L\to P} \times m_P \vec{a}_{P/I} + \vec{r}_{L\to X} \times m_T \vec{a}_{X/I} \right) = \vec{I}_S \bullet \sum M^L_{System} \ , \tag{16}$$

$$\vec{J}_S \bullet \left(\frac{{}^I d\vec{H}^P_{B/I}}{dt} + \frac{{}^I d\vec{H}^X_{T/I}}{dt} + \vec{r}_{L\to P} \times m_P \vec{a}_{P/I} + \vec{r}_{L\to X} \times m_T \vec{a}_{X/I} \right) = \vec{J}_S \bullet \sum M^L_{System} \ , \tag{17}$$

$$\vec{K}_S \bullet \left(\frac{{}^I d\vec{H}^X_{T/I}}{dt} + \vec{r}_{L\to X} \times m_T \vec{a}_{X/I} \right) = -f_{Input} BLc_\gamma + \vec{K}_S \bullet \mathbb{S}\left(\vec{r}_{L\to X}\right) \mathbb{C}_S \left(\vec{W}_T\right) + k_T \gamma + k_D \dot{\gamma} \ , \tag{18}$$

and

$$\begin{aligned} \vec{K}_S \bullet \left(\frac{{}^I d\vec{H}^P_{B/I}}{dt} + \vec{r}_{L\to P} \times m_P \vec{a}_{P/I} \right) = \ & f_{Input} BLc_\gamma + \vec{K}_S \bullet \mathbb{S}\left(\vec{r}_{L\to P}\right) \mathbb{C}_S \left(\vec{W}_P\right) - k_T \gamma - k_D \dot{\gamma} + \vec{K}_S \\ & \bullet \mathbb{C}_S \left(\Sigma M^L_P\right), \end{aligned} \tag{19}$$

where, as before, $c_\gamma = \cos(\gamma)$. Note that equation 18 equates the time rate of change of the angular momentum of the ITM-Beam to the total moment applied to the ITM-Beam. Equation 19 equates the time rate of change of the angular momentum of the projectile to the total moment applied to the projectile.

Several intermediate expressions will be useful in deriving the rotational dynamic equations in the body-fixed *S* frame. First, note that the well-known two points fixed on a rigid body formula yields the relationship

$$\vec{a}_{X/I} = \vec{a}_{C/I} + \frac{m_P}{m}\left[\vec{\alpha}_{B/I} \times \vec{r}_{P\to L} + \vec{\alpha}_{T/I} \times \vec{r}_{L\to X} + \vec{\omega}_{B/I} \times \left(\vec{\omega}_{B/I} \times \vec{r}_{P\to L} \right) + \vec{\omega}_{T/I} \times \left(\vec{\omega}_{T/I} \times \vec{r}_{L\to X} \right) \right]. \tag{20}$$

Equation 20 is used to expand $\vec{a}_{X/I}$ in terms of known quantities and state derivatives. Also, using the definition of the system center of mass, it can be shown through algebraic manipulation that

$$\vec{r}_{L\to P} \times m_P \vec{a}_{P/I} + \vec{r}_{L\to X} \times m_T \vec{a}_{X/I} = \vec{r}_{L\to P} \times m \vec{a}_{C/I} + \vec{r}_{P\to X} \times m_T \vec{a}_{X/I} \ . \tag{21}$$

Equation 21 is also used to expand the cross-product terms on the left-hand side of equations 16 and 17 in terms of known quantities and state derivatives.

Equations 16–19 can be expanded using the expressions in equations 20 and 21 and rearranged to form a 4 × 4 system of equations given by

$$\begin{bmatrix} A_{11} & A_{12} & A_{13} & A_{14} \\ A_{21} & A_{22} & A_{23} & A_{24} \\ A_{31} & A_{32} & A_{33} & A_{34} \\ A_{41} & A_{42} & A_{43} & A_{44} \end{bmatrix} \begin{bmatrix} \dot{\tilde{p}} \\ \dot{\tilde{q}} \\ \dot{\tilde{r}} \\ \ddot{\gamma} \end{bmatrix} = \begin{bmatrix} B_1 \\ B_2 \\ B_3 \\ B_4 \end{bmatrix}. \tag{22}$$

In equation 22, rows 1–4 correspond to equations 18, 19, 17, and 16, respectively. The full expressions for the values of the *A* matrix and *B* vector are lengthy and provided in appendix A. The set of equations given by 7, 9, 10, 15, and 22 constitutes the equations of motion for the ITM-Beam projectile. Given a known set of initial conditions, these 14 scalar equations are numerically integrated forward in time using a fourth-order Runge-Kutta algorithm to obtain a single trajectory.

2.3 Description of Controller

To create trajectory alterations, the ITM-Beam must be moved in a prescribed manner. The control law is formulated based on a feedback linearization technique (*11*), which assumes full-state feedback. To compute the control force, $\boldsymbol{f}_{input}$, required to deflect the ITM-Beam to the desired angle, use the following:

$$\begin{aligned} \boldsymbol{f}_{input} = \frac{-1}{\boldsymbol{BLc}_{\gamma}} \left[\boldsymbol{B}_{FLC} - \boldsymbol{A}_{11}\dot{\tilde{\boldsymbol{p}}} - \boldsymbol{A}_{12}\dot{\tilde{\boldsymbol{q}}} - \boldsymbol{A}_{13}\dot{\tilde{\boldsymbol{r}}} - \boldsymbol{A}_{14}\ddot{\gamma} \right] - \boldsymbol{K}_0 \ddot{\gamma}_{\boldsymbol{command}} \\ - \boldsymbol{K}_1 \left(\dot{\gamma}_{\boldsymbol{command}} - \dot{\gamma} \right) - \boldsymbol{K}_2 \left(\gamma_{\boldsymbol{command}} - \gamma \right). \end{aligned} \tag{23}$$

Note that $\boldsymbol{B}_{FLC}$ is defined in appendix A and derived from equation 18. Likewise, $\boldsymbol{A}_{11}, \boldsymbol{A}_{12}, \boldsymbol{A}_{13}$, and $\boldsymbol{A}_{14}$ are from equation 18 and provided in appendix A. Note that equation 18 is used to compute the feedback linearization control rather than equation 19 since equation 19 would require feedback of aerodynamic loads. This is a complicated task and can be avoided by using equation 18 instead.

The commanded deflection angle, $\gamma_{\boldsymbol{command}}$, is generated by synchronizing ITM-Beam movement with the projectile roll angle. This is done by setting

$$\gamma_{\boldsymbol{command}} = \boldsymbol{\sin}^{-1}\left(-\frac{\boldsymbol{A}}{\boldsymbol{BL}} \boldsymbol{\cos}\left(\phi + \phi_{\boldsymbol{T}} \right) \right), \tag{24}$$

where *A* is the magnitude of oscillation of point *X* from the cavity center and ϕ_T is a trim angle used to define the plane of control. Derivatives of equation 24 are computed analytically and used in equation 23. Note that the feedback linearization controller is developed and used

within the simulation solely to create the prescribed motion of the ITM-Beam for control authority analysis and determination of power requirements. In this case, its purpose is to match the ITM-Beam oscillation frequency to the projectile roll rate within the simulation.

2.4 Description of Electromagnetic Actuator Control System

A zoom view of the ITM-Beam mechanism is shown in figure 2. Two electromagnets, each at opposite ends of the cavity, exert force on the fixed magnet at the end of the ITM-Beam.

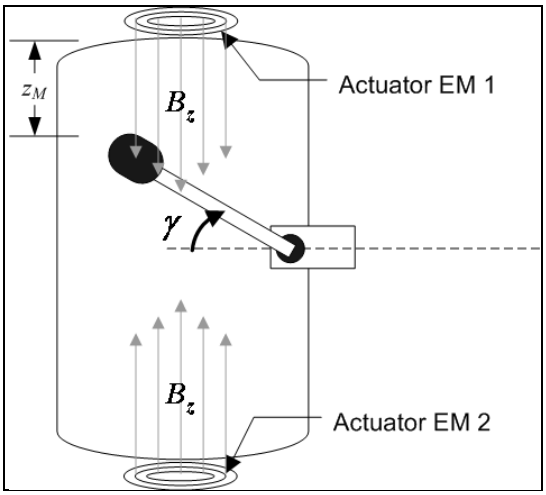

Figure 2. Zoom view of the ITM-Beam system.

The force exerted on a fixed magnetic dipole *DM* is given by Purcell (*12*) as

$$\boldsymbol{f_{input}} = \boldsymbol{DM}\,\frac{\partial \boldsymbol{B}_z}{\partial \boldsymbol{z}_M}\ . \tag{25}$$

The magnetic dipole moment per unit mass is a unique property of a material, with units joules/tesla/slug. For example, assuming the ITM is made of magnetized iron and using an ITM-Beam mass of m_t = 0.05 slugs, the dipole moment is found to be *DM* = 171.5 J/T. The quantity $\frac{\partial \boldsymbol{B}_z}{\partial \boldsymbol{z}_M}$ can be found by first recognizing that the magnetic field, $\boldsymbol{B}_z$, of an iron core solenoid is given by the expression

$$\boldsymbol{B}_z = \frac{\boldsymbol{I}_E\,\mu \boldsymbol{k} \boldsymbol{n}}{2}\left[\frac{-\boldsymbol{z}_M}{\sqrt{\boldsymbol{z}_M^2 + \boldsymbol{b}^2}} + \frac{\boldsymbol{z}_M + \boldsymbol{L}_A}{\sqrt{\left(\boldsymbol{z}_M + \boldsymbol{L}_A\right)^2 + \boldsymbol{b}^2}}\right], \tag{26}$$

where I_E is the current through the electromagnet, μ is the magnetic constant ($4\pi \times 10^{-7}$ N/A^2), z_M is the distance from the endpoint of the ITM beam to the nearest electromagnet actuator, k is the dimensionless relative permeability of iron (200 at a magnetic flux density of 0.002 W/m^2), n is the number of coils per meter, b is the radius of the solenoid, and L_A is the length of the solenoid. For all the following cases, values of 3, 2, and 10000 cm were used for b, L, and n, respectively. Taking the derivative of equation 26 with respect to z_M,

$$\frac{\partial B_z}{\partial z_M} = \frac{I_E \mu k n}{2}\left[\frac{-1}{\sqrt{z_M^2 + b^2}} + \frac{z_M^2}{\left(z_M^2 + b^2\right)^{3/2}} + \frac{1}{\sqrt{\left(z_M + L_A\right)^2 + b^2}} - \frac{\left(z_M + L_A\right)^2}{\left(\left(z_M + L_A\right)^2 + b^2\right)^{3/2}}\right]. \quad (27)$$

At each timestep, control force is computed using the feedback linearization. Knowing the magnetic dipole moment and required control force, the quantity $\frac{\partial B_z}{\partial z_M}$ is computed at each timestep using equation 25. Then, knowing the position of the ITM-Beam with respect to the actuators, the current required can be computed at each timestep by rearranging equation 27 so that

$$I_E = \frac{2}{k \mu n}\left[\frac{-1}{\sqrt{z_M^2 + b^2}} + \frac{z_M^2}{\left(z_M^2 + b^2\right)^{3/2}} + \frac{1}{\sqrt{\left(z_M + L_A\right)^2 + b^2}} - \frac{\left(z_M + L_A\right)^2}{\left(\left(z_M + L_A\right)^2 + b^2\right)^{3/2}}\right]^{-1} \frac{\partial B_z}{\partial z_M}. \quad (28)$$

Note that the electromagnet dimensions used in equation 28 are comparable to dimensions for commercially available iron-core electromagnets.

2.5 Description of Example Projectile

The example projectile used in the following simulations is a representative fin-stabilized projectile. Relevant example projectile and ITM-Beam dimensional and mass properties are outlined in table 1. The hinge point is 0.9 ft behind the projectile mass center (P), and the ITM-Beam oscillation amplitude is given by $BL\sin(\gamma_{max}) = 0.157$ ft, unless otherwise specified. In the following cases, the projectile is traveling through a standard atmosphere, with no atmospheric wind.

Table 1. Relevant example projectile and ITM-Beam properties.

Projectile Mass (slugs)	1.206
ITM-Beam Mass (slugs)	0.05
Projectile Reference Diameter (ft)	0.344
Projectile Mass Center Position Measured Along Stationline (ft)	1.18
Projectile Roll Inertia (slugs-ft^2)	0.0278
Projectile Pitch Inertia (slugs-ft^2)	0.6291
ITM-Beam Length (ft) (*BL*)	0.3

3. Results

An example trajectory of the ITM-Beam projectile is compared to an example trajectory of a projectile equipped with a strictly translating internal mass for model validation purposes. The translating mass projectile's dynamic equations are given in reference *10*, and a previously validated model of this system was used for trajectory predictions. A diagram of the translating mass projectile is provided in appendix B. Initial conditions used for the example trajectory were x = 0.0 ft, y = 0.0 ft, z = 0.0 ft, u = 2821.0 ft/s, v = 0.0 ft/s, w = 0.0 ft/s, ϕ = 1.5707 rad, θ = 0.05 rad, ψ = 0.0 rad, p = 5.0 rad/s, q = 0.0 rad/s, and r = 0.0 rad/s. The feedback linearization gains were $\boldsymbol{K}_0 = 0.001$, $\boldsymbol{K}_1 = 1000.0$, and $\boldsymbol{K}_2 = 5 \times 10^5$. In the following cases, the ITM-Beam oscillation frequency is locked to the projectile roll rate. Figures 3–6 show the trajectories for the ITM-Beam projectile, translating mass projectile, and the rigid projectile with no internal moving mass (denoted "Rigid 6DOF"). The two translating mass trajectories are generated solely to demonstrate control authority and validate the ITM-Beam simulation; thus, both controlled rounds are commanded to maximum possible deflection. Notice that the trajectories of the internal mass projectiles match nearly identically, even though the dynamic equations for the two systems are significantly different. The correlation between these two models serves as validation of the ITM-Beam simulation.

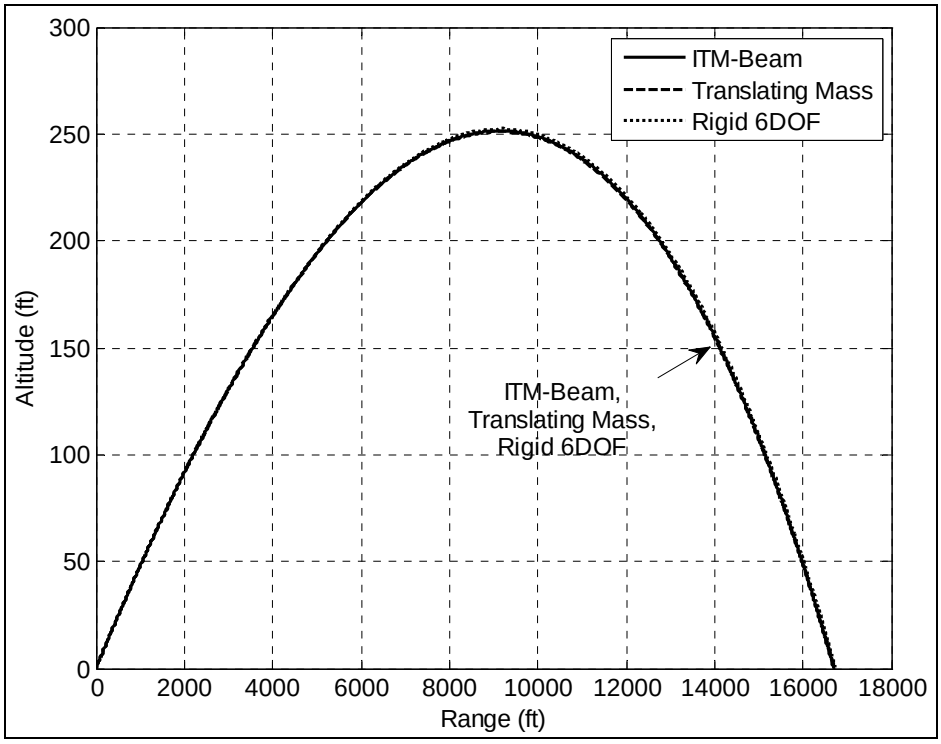

Figure 3. Altitude vs. range for example trajectory.

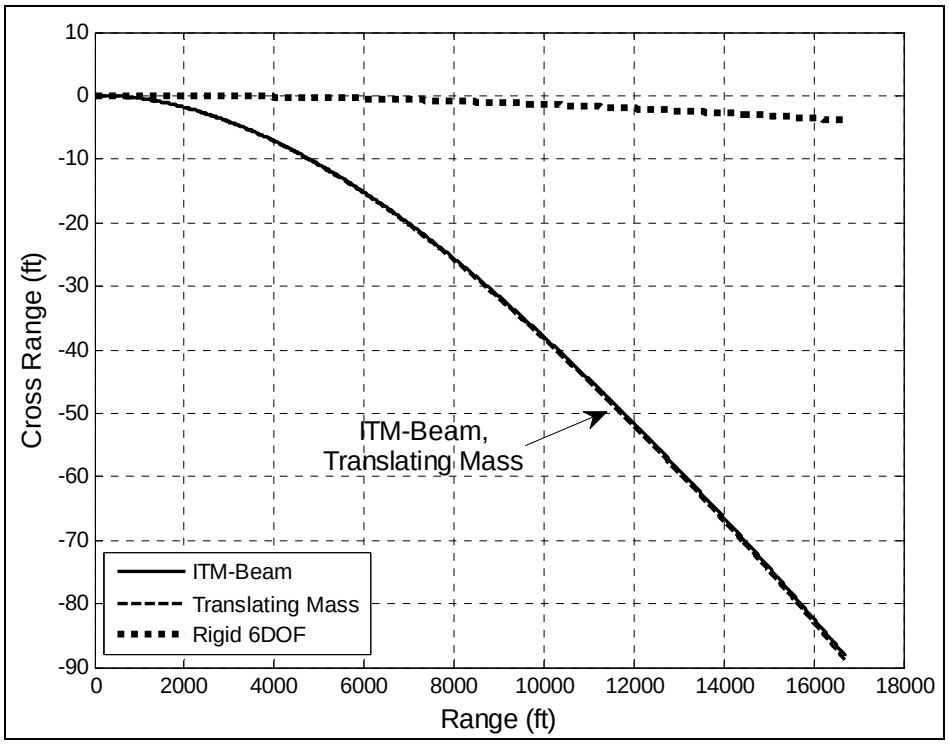

Figure 4. Cross range vs. range for example trajectory.

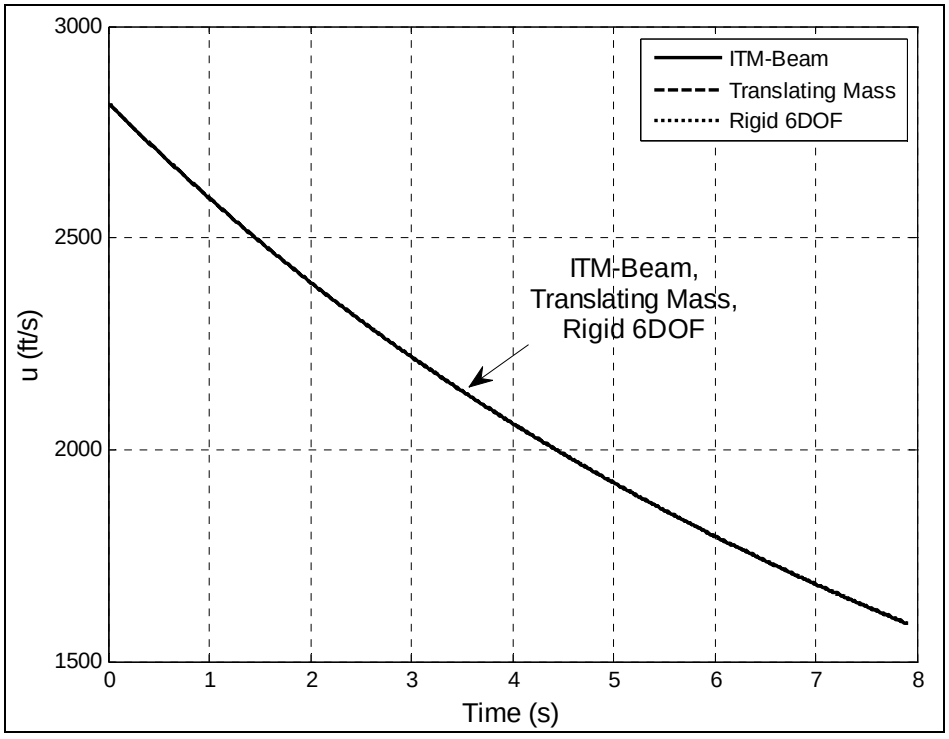

Figure 5. Velocity (u) vs. time for example trajectory.

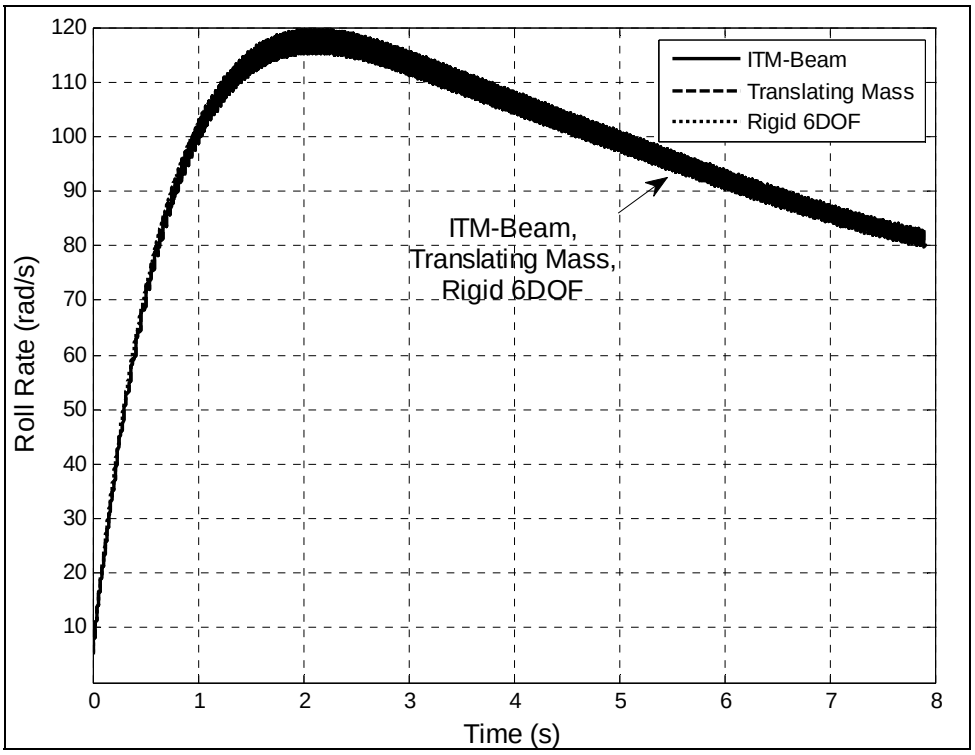

Figure 6. Roll rate vs. time for example trajectory. The thick lines represent high-frequency oscillations, which occur only for the ITM-Beam and translating mass case.

Figure 7 shows a selected time history of ITM displacement from the projectile centerline. For the ITM-Beam projectile, this displacement, $\boldsymbol{s}_x$, is given by

$$\boldsymbol{s}_x = \boldsymbol{BL}\sin(\gamma) \ . \tag{29}$$

Notice that the two time histories for ITM displacement shown in figure 7 are nearly identical. A control-force time history for an example ITM-Beam projectile simulation can be used together with an ITM displacement time history to generate a time history of current required for each electromagnetic actuator. This is accomplished using the procedure outlined in equations 25–28. Furthermore, this current time history can be integrated to produce the total charge required for a given example flight in A/s. This value for total charge can be used to size the battery for the ITM-Beam control system. The total charge required for the example flight shown previously was 13.5 A/s. Note that this number is relatively large since the spring and damper coefficient values have not been optimized for this preliminary example case.

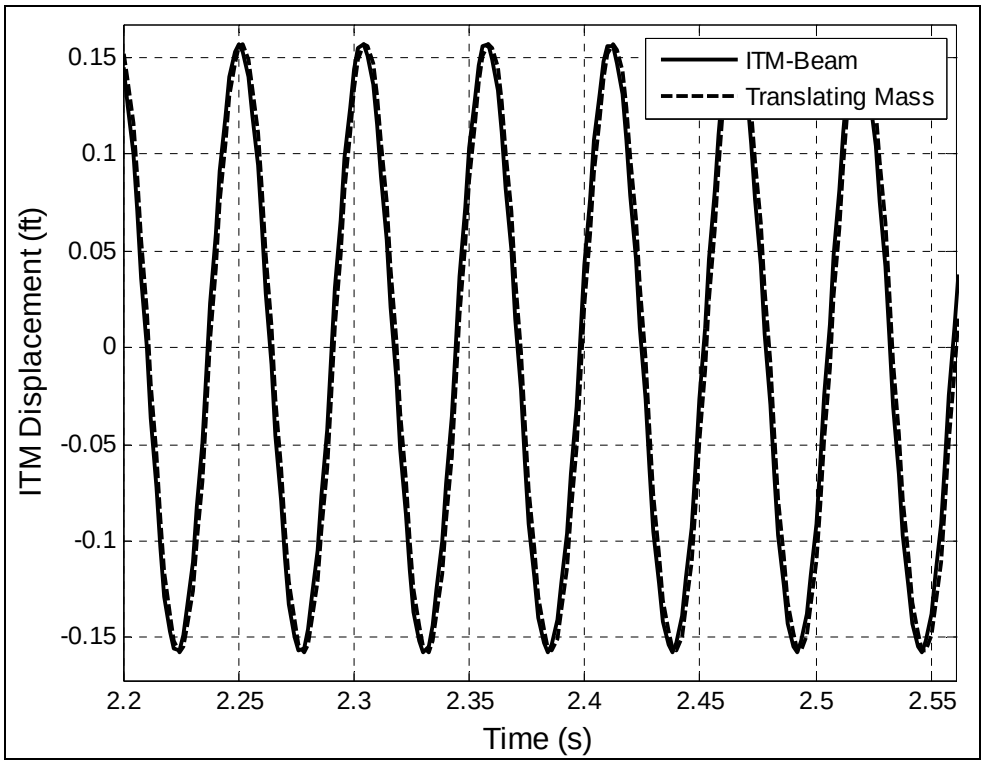

Figure 7. Selected time history of ITM displacement from projectile centerline.

Figure 8 shows a segment of the current time history for the example ITM-Beam simulation used previously. Notice that $\boldsymbol{f}_{input}$ (labeled "Force" in the plot) and the ITM displacement, $\boldsymbol{s}_x$, are shown on the same plot as the current time history to demonstrate the phase relationships between current, input force, and ITM displacement. When the ITM-Beam is displaced in the positive $\vec{I}_s$ direction ($\boldsymbol{s}_x$ positive), electromagnet EM 1 shuts off, and EM 2 is responsible for control. Likewise, when the ITM-Beam is displaced in the negative $\vec{\boldsymbol{I}}_s$ direction ($\boldsymbol{s}_x$ negative), electromagnet EM 2 shuts off, and EM 1 is responsible for control. This scheme takes advantage of the fact that the electromagnets are more effective when the ITM is at close range. Since current required is a nonlinear function of distance to the ITM and control force required, the current time history is not sinusoidal like the ITM displacement and control-force time histories.

The length of the ITM-Beam has a significant impact on the force required to move the beam in a prescribed fashion. From equation 18, the external moment exerted on the ITM-Beam by the actuators in the $\vec{\boldsymbol{K}}_s$ direction about point *L* is given by

$$\vec{K}_S \bullet \vec{M}^{L}_{Beam} = -f_{Input} BLc_{\gamma} \ . \tag{30}$$

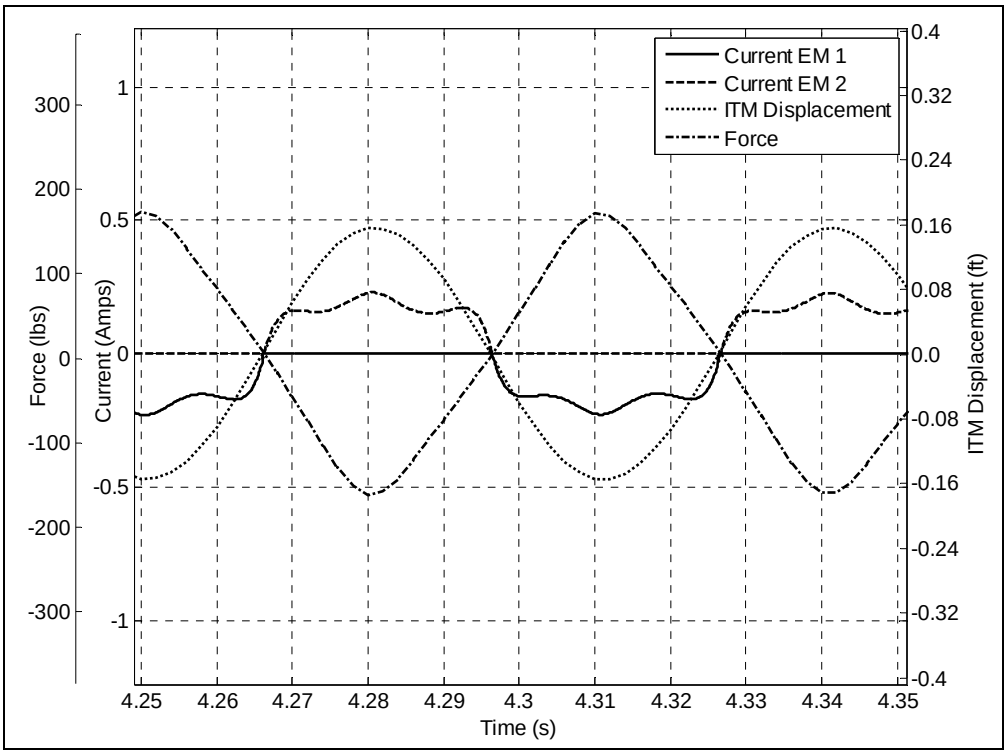

Figure 8. Segment of current vs. time for ITM-Beam actuators.

Therefore, the input force required to exert a given control moment on the ITM-Beam varies inversely with beam length. In addition, for a given maximum ITM displacement, $\boldsymbol{s}_x$, the maximum angular displacement, $\gamma_{\max}$, varies inversely with beam length. Trade studies verified these results using example simulations with various beam lengths. The maximum ITM displacement from the projectile centerline was $\boldsymbol{s}_x = 0.157$ ft for all cases. Figures 9 and 10 show maximum angular displacement and average force required, respectively, as a function of beam length. Notice that as beam length increases, maximum angular displacement and average force required decrease. The average control-force reduction with increased beam length occurs due to the increased "efficiency" of the ITM-Beam actuators (i.e., the same control moment requires less control force for a larger beam length).

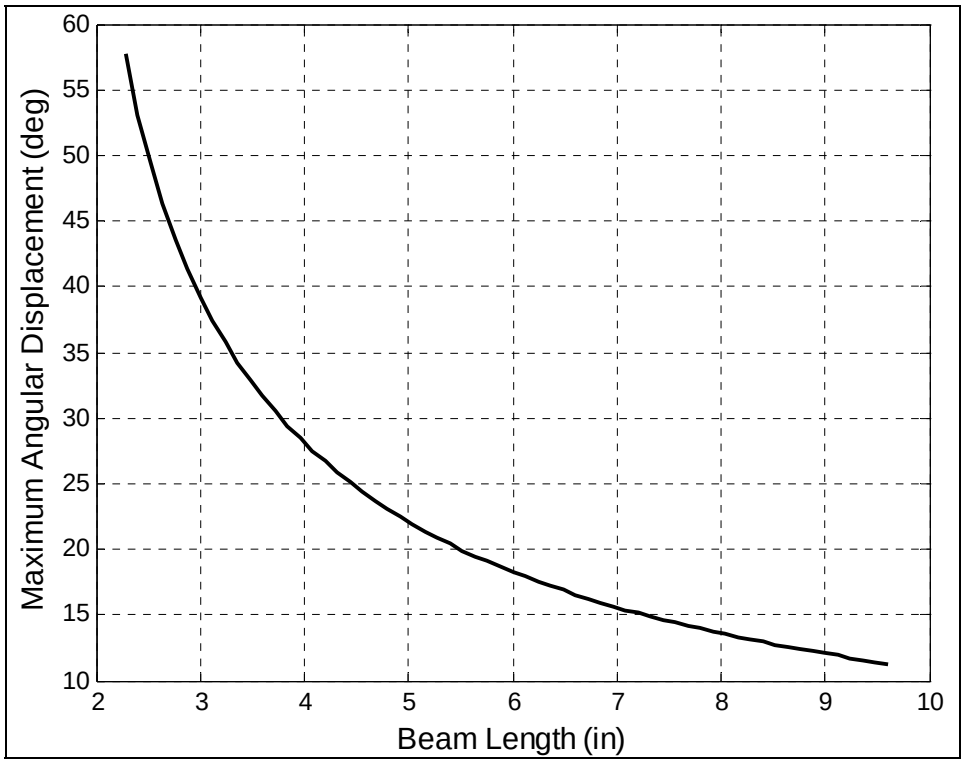

Figure 9. Maximum angular displacement vs. beam length.

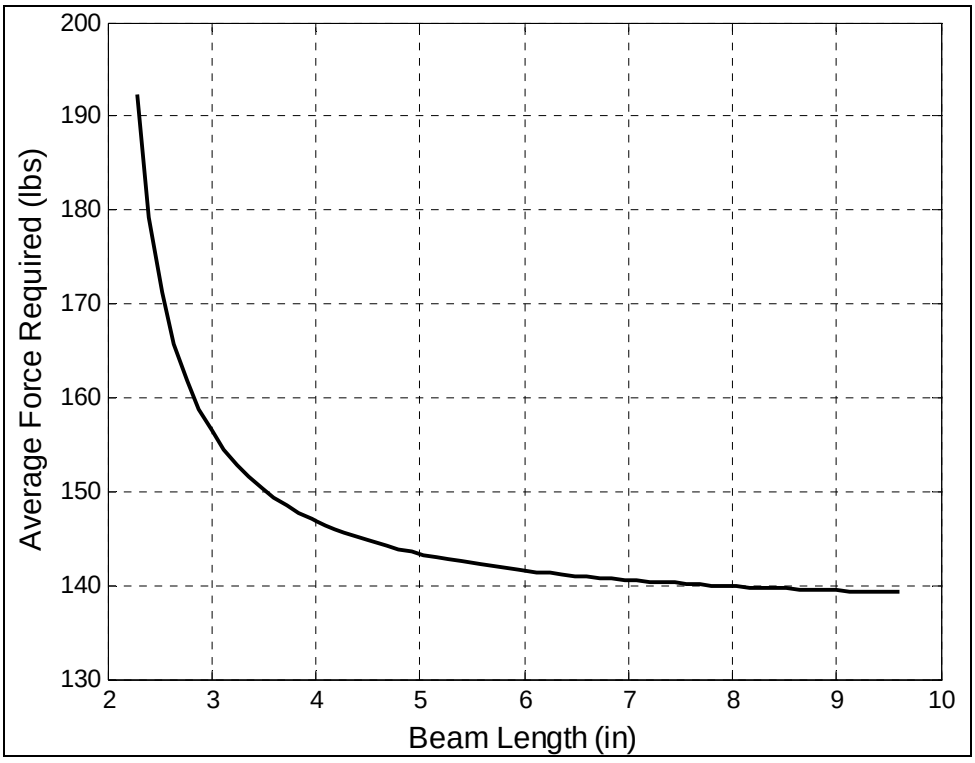

Figure 10. Average force required vs. beam length.

As outlined previously, the ITM-Beam system is a dynamic model used to represent a fixed-free elastic beam. The rigid ITM-Beam is attached to the projectile at point *L* with a torsional spring and torsional damper to model the elastic beam's vibrational properties. A trade study examines how force and power requirements vary with different spring and damping coefficients. Once an optimum spring and damper coefficient are determined, they can be used to identify the proper elastic properties of the fixed-free beam for a prototype system.

The performance of the system is examined for a range of torsional spring constants and damping ratios for the example projectile rolling at a steady-state rate of ~128 rad/s. The projectile trajectory is simulated for a 2-s flight with no gravity. This simplified flight profile is used solely to establish the correlation between spring and damper parameters and average force, average power, and total battery charge required. Figure 11 shows the projectile roll-rate time history for this flight profile. The high-frequency oscillation of the roll rate occurs at the mass oscillation frequency. This is due to the continually changing axial moment of inertia of the projectile as the mass translates. When the translating mass travels farther from the centerline, axial inertia grows and roll rate decreases due to conservation of angular momentum. Likewise, when the translating mass returns toward the centerline, axial inertia decreases and the roll rate increases.

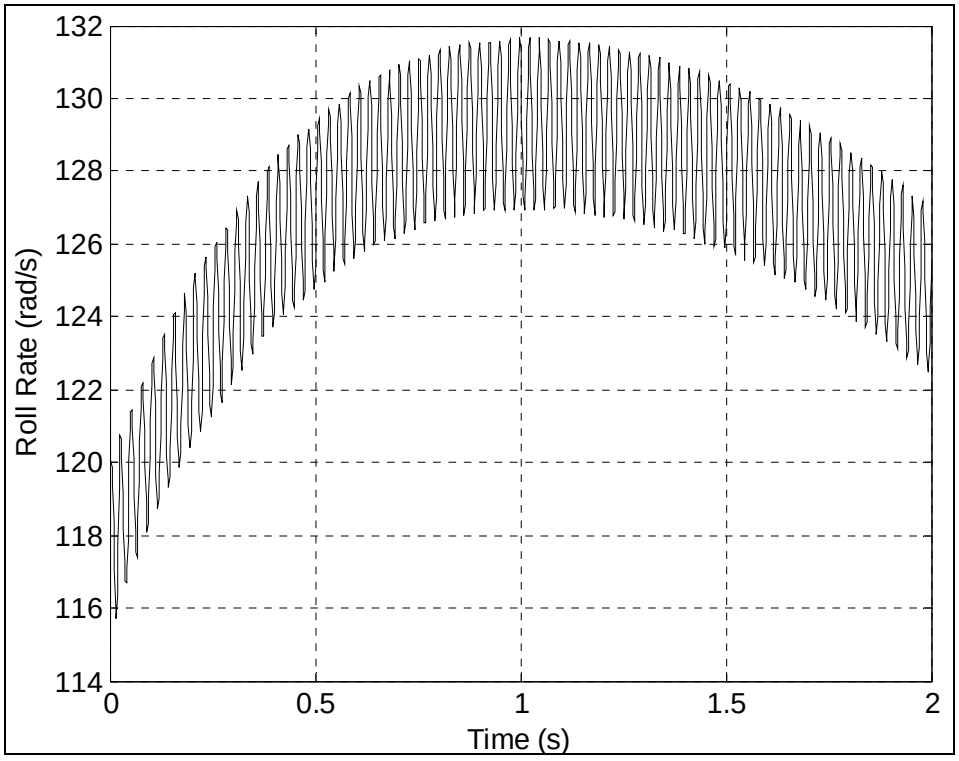

Figure 11. Roll rate vs. time for example simulation.

Figures 12–14 show the effect of spring and damper coefficients on average force, average power, and total battery charge required. In figure 12, it can be clearly seen that an optimum torsional spring constant exists in which the spring-mass-damper system of the ITM-Beam operates near resonance with the projectile roll rate. These peaks are not as sharp as typical spring-mass-damper resonant peaks due to the fact that the projectile roll rate varies over time. However, note that significant reductions in force are achieved if the spring constant is placed near its optimum value and damping is lowered as much as possible. These reductions in force are mirrored by reductions in average power and total charge required, resulting in significantly smaller battery sizes.

A similar study examines the same spring-mass-damper parameters for a full flight profile of the example projectile using the same initial conditions as those used in the first example study. Figures 15–17 show that as in the partial flight profile case, optimal spring coefficients can be found.

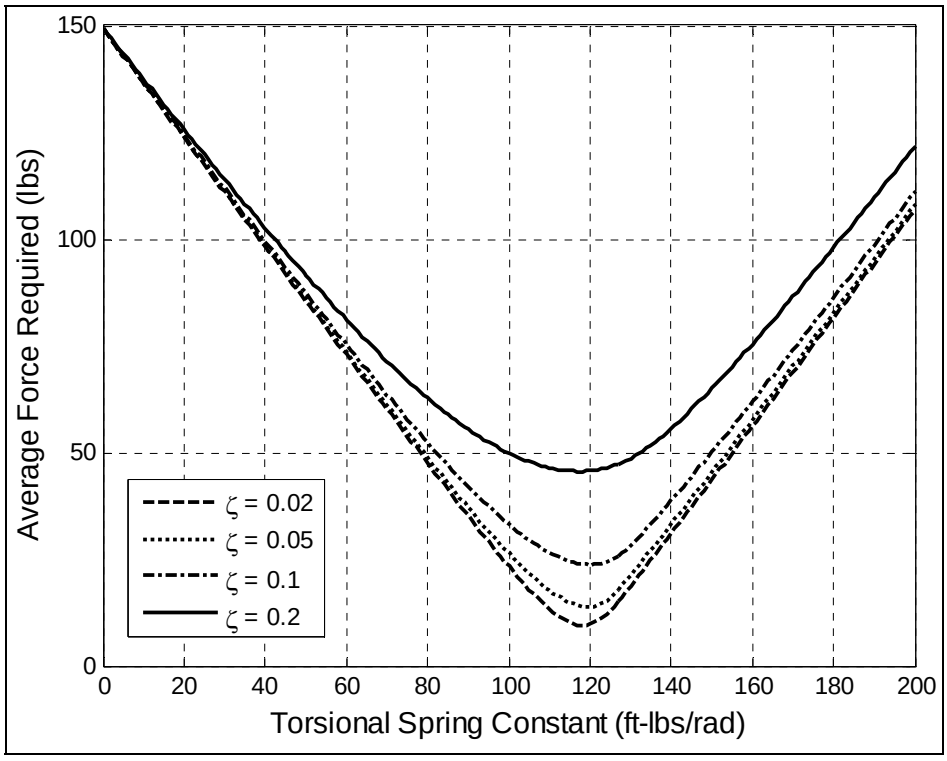

Figure 12. Average force required vs. torsional spring constant, partial flight profile.

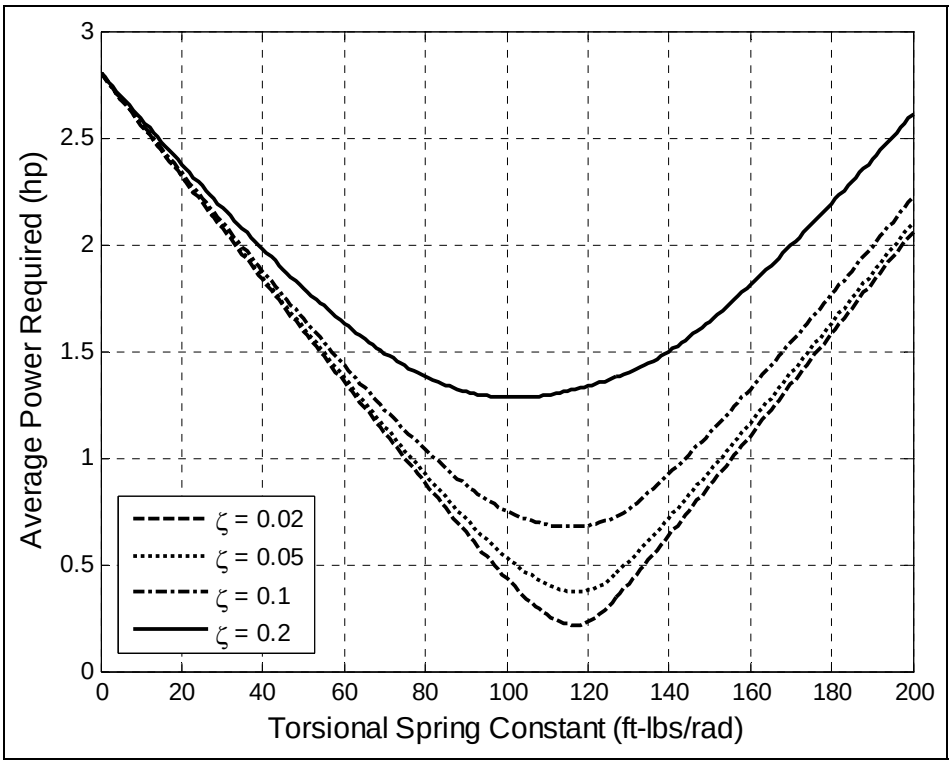

Figure 13. Average power required vs. torsional spring constant, partial flight profile.

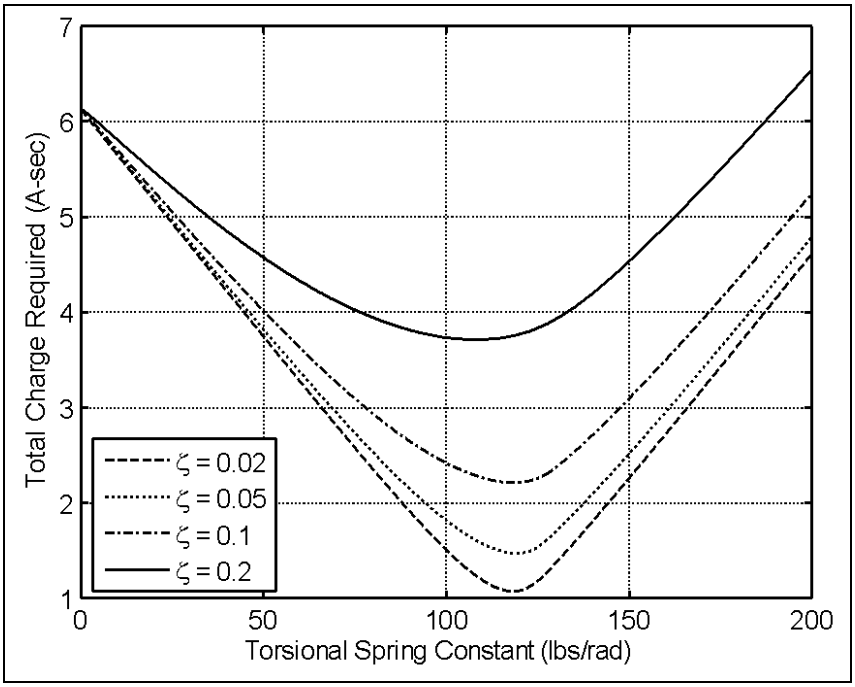

Figure 14. Total charge required vs. torsional spring constant, partial flight profile.

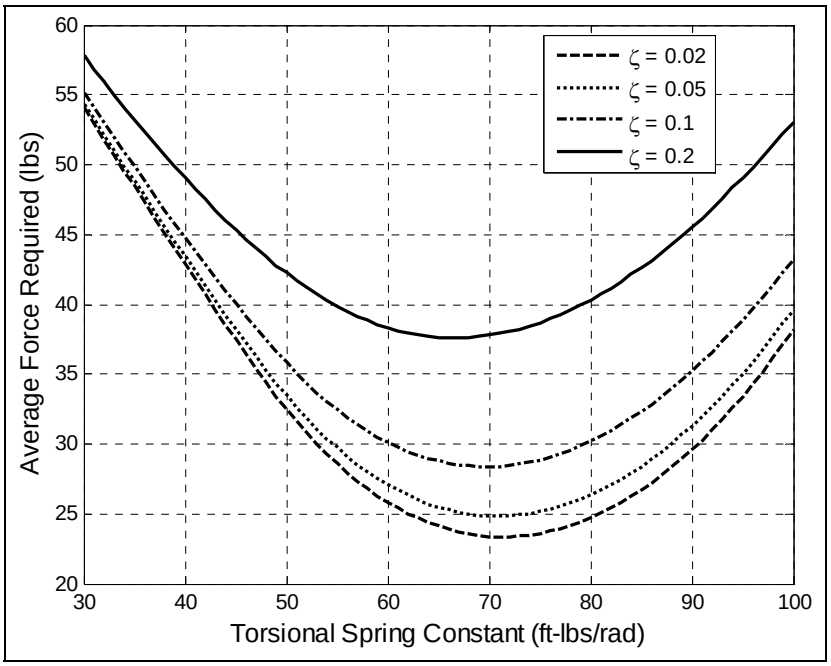

Figure 15. Average force required vs. torsional spring constant, full flight profile.

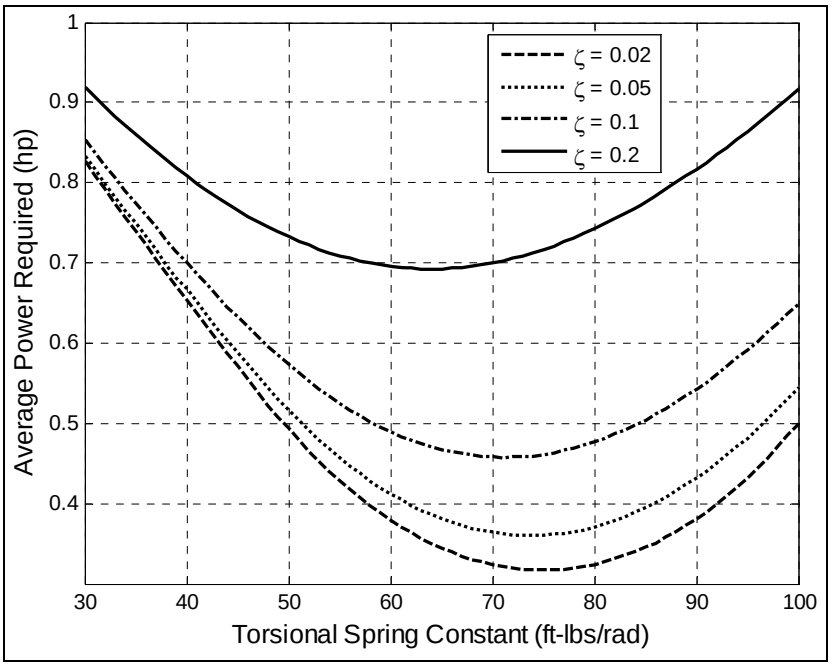

Figure 16. Average power required vs. torsional spring constant, full flight profile.

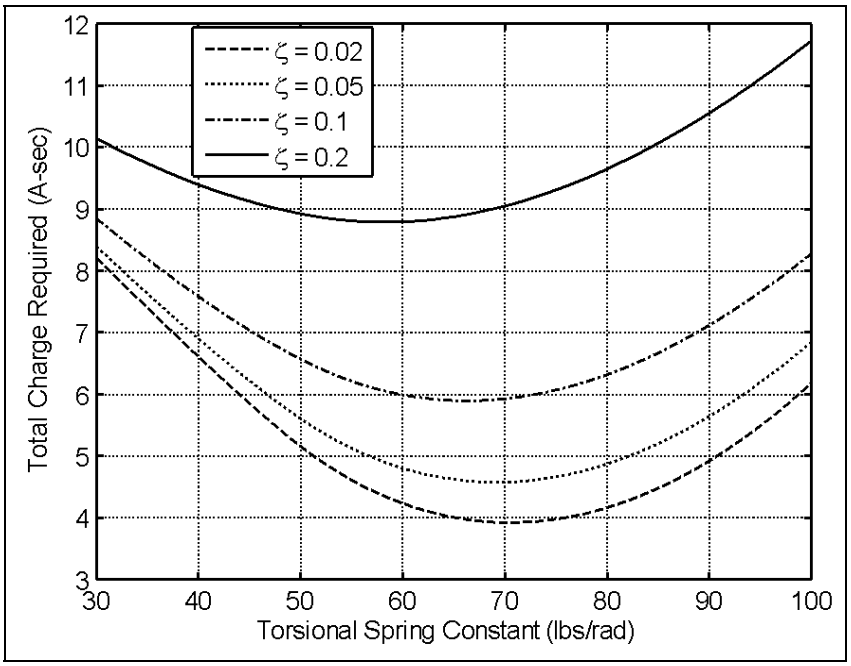

Figure 17. Total charge required vs. torsional spring constant, full flight profile.

However, the results for the partial flight profile have a significantly sharper peak than the results for the full flight profile. This is because, as shown in figure 6, roll rate of the projectile varies between 5 rad/s initially and a final value of ~80 rad/s. This large variation in roll rate means that the spring coefficient is only optimized for a very short period of the overall flight, and the broad peaks shown in figures 15–17 result. To demonstrate this, figure 18 shows a current time history for an example full flight trajectory using $\boldsymbol{k_T}$ = 70.0 lb/rad and $\boldsymbol{k_D}$ = 0.05 lb/rad/s. Note that the spring constant is optimized for the projectile roll rate ~1 s into flight and once again after spin decay occurs ~7 s into the flight.

Despite the broad nature of the peaks shown in figures 15–17, significant size and weight savings can be achieved using the proper spring constants in the form of smaller batteries. As shown in figure 17, batteries with a total charge of less than 5 A/s may be used for systems with optimal spring coefficients and low damping ratios. Furthermore, figure 18 shows that reasonable maximum current levels, on the order of 150 mA, can be expected with an optimized system.

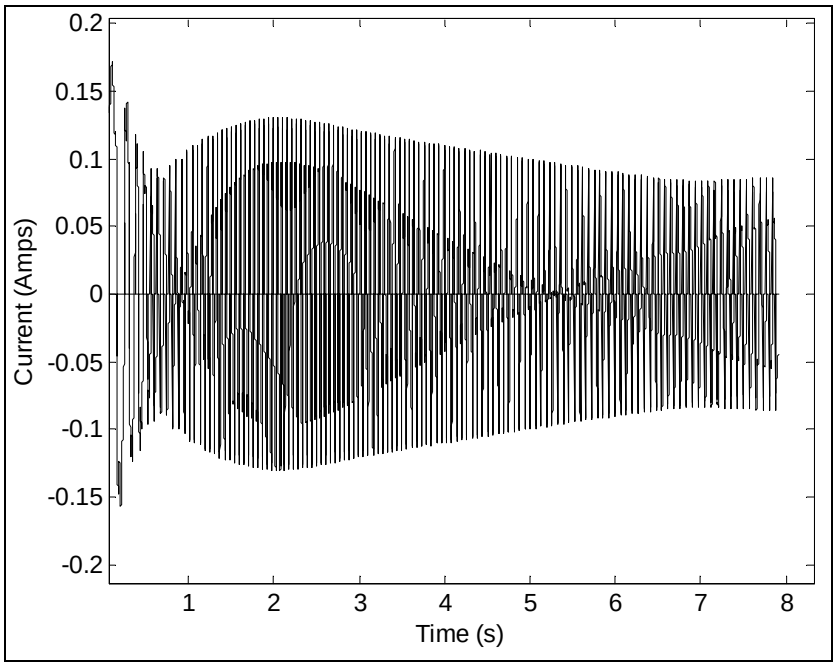

Figure 18. Current through actuators vs. time for example full flight trajectory.

Average force levels and, therefore, total charge required can be decreased even further by actively changing the elastic properties of the beam during flight. A fixed-free cantilever beam like that used in this system has a first vibrational mode shape of

$$\boldsymbol{S}_x = \mathbf{sin}\left(\frac{\pi \boldsymbol{x}_B}{2\boldsymbol{BL}}\right), \tag{31}$$

where $\boldsymbol{x}_B$ is the distance along the beam. The natural frequency of the first vibrational mode is

$$\omega_n = \frac{\pi}{2\boldsymbol{BL}}\sqrt{\frac{\boldsymbol{E}}{\rho}}, \tag{32}$$

where E is the modulus of elasticity of the material and ρ is the density of the beam (*13*). By changing the modulus of elasticity, it is therefore possible to tune the natural frequency of the cantilever beam to a desired value. Recent investigations into smart materials (*14–17*), specifically, materials used in tunable vibration absorbers, have shown that various methods can be used to actively alter a material's modulus of elasticity, allowing the beam's torsional spring constant to be actively optimized during flight as the projectile roll rate changes. This would allow the ITM-Beam system to operate with the lowest possible power through the entire flight, yielding further reductions in battery size.

To investigate this, several example simulations were run. The first set simulated the projectile for the full flight using the optimum spring constants obtained from figure 17. This produced the least possible battery charge required for the ITM-Beam system, with a fixed spring constant for each damping ratio considered. The second set of simulations included a roll-rate feedback mechanism. In these cases, at specific points throughout the flight, the torsional spring and damping coefficients of the ITM-Beam were adjusted to match the roll rate. Figure 19 shows how the torsional spring constant was adjusted for an example flight with $\zeta = 0.05$. Note that the curve in figure 19 has the same qualitative shape as the roll rate time history shown in figure 6. Table 2 summarizes the results of the two sets of simulations with the fixed torsional spring and variable torsional spring constants. Note that in the variable torsional spring cases, the torsional damping coefficient k_D was adjusted slightly to keep the damping ratio ζ constant. Figure 20 demonstrates that implementing the roll-rate feedback system saves ~1 A/s of charge for all damping ratios considered (34.4% decrease in battery size for $\zeta = 0.02$, 28.1% decrease for $\zeta = 0.05$, 20.4% for $\zeta = 0.1$, and 11.2% for $\zeta = 0.2$).

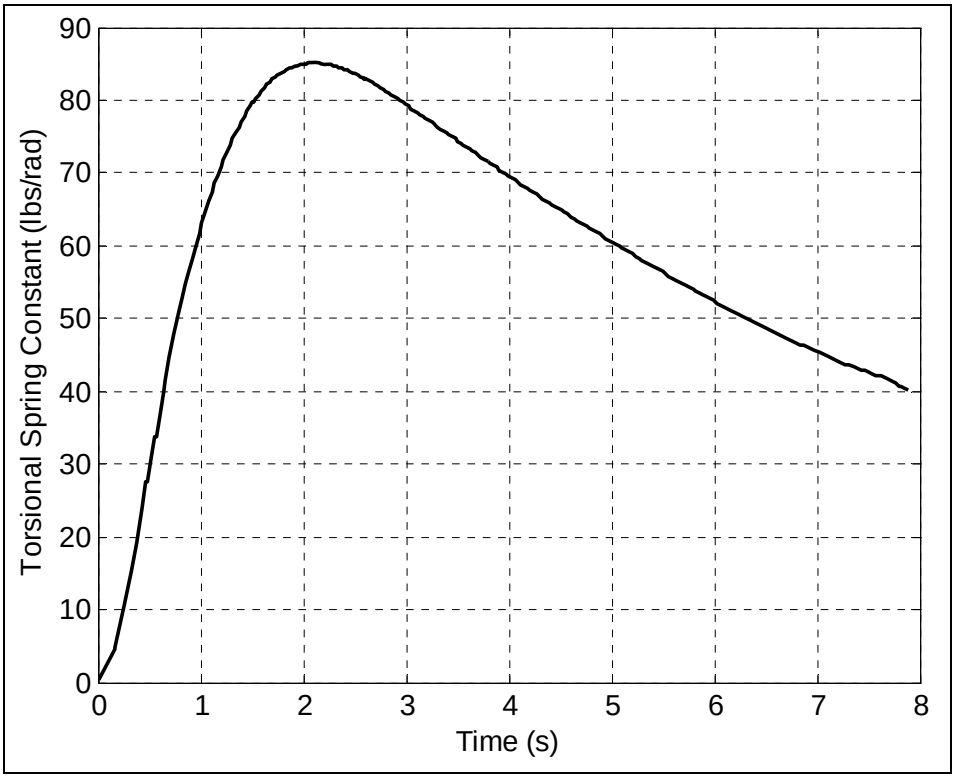

Figure 19. Torsional spring constant vs. time for roll-rate feedback system, $\zeta = 0.05$.

Table 2. Performance evaluation of roll-rate feedback system.

Damping Ratio ζ	Optimum k_T for No Feedback Case	Charge Required (A/s)		Percentage Decrease in Charge Required With Feedback
		No Feeback (Constant k_T)	Feedback (Variable k_T)	
0.02	71	3.924	2.576	34.4%
0.05	69	4.576	3.287	28.1%
0.1	67	5.895	4.692	20.4%
0.2	58	8.786	7.798	11.2%

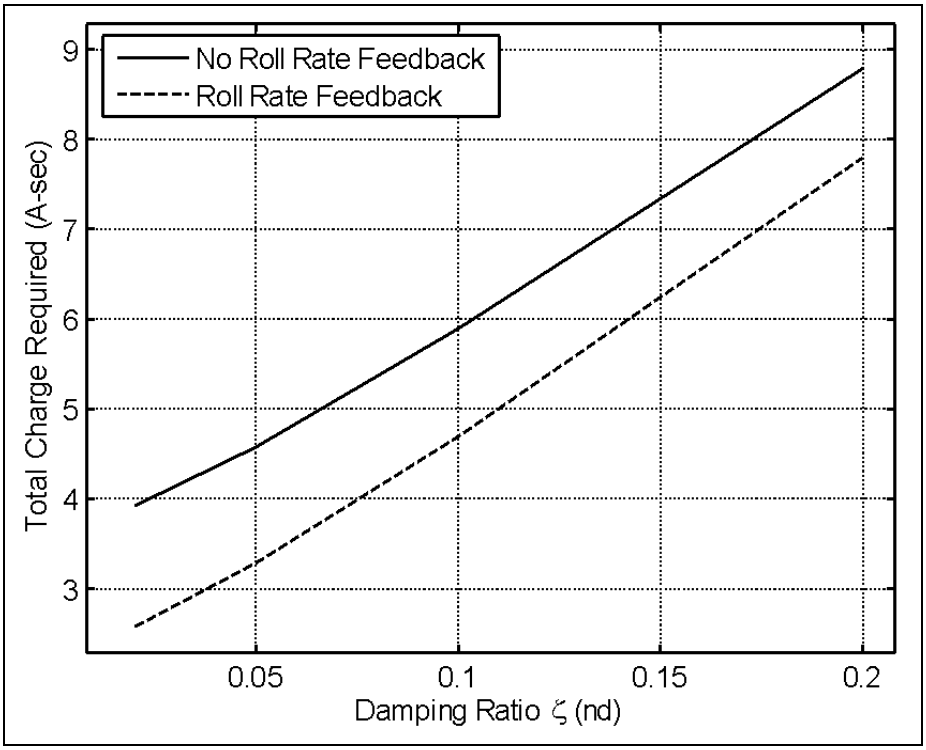

Figure 20. Total charge required vs. damping ratio for constant and variable k_T cases.

4. Conclusion

A conceptual design for a projectile equipped with a controllable internal mass is proposed using a cantilever beam configuration. The system is designed to minimize moving parts and exploit the beam's elastic properties, thereby creating a robust mechanism that minimized power requirements. A dynamic model of the configuration is developed, as is a model of the electromagnetic actuator system to study current requirements and battery size. Example simulations show that useful control authority is generated with this projectile control mechanism, matching the results from earlier studies of projectiles with internal translating mass

control. Furthermore, by tuning the natural frequency of the vibrating beam to the projectile roll rate, significant reductions in power requirements are achieved on the order of 60%. Power reductions can be further realized with active tuning of the beam's elastic properties during flight. Battery size requirements to power the actuator are modest, with several commercial-off-the-shelf options available. The internal oscillating beam configuration shows promise as a viable, cost-effective, reliable projectile control mechanism.

5. References

1. Soper, W. Projectile Instability Produced by Internal Frictio. *AIAA Journal* **1978**, *16* (1), 8–11.
2. Murphy, C. Influence of Moving Internal Parts on Angular Motion of Spinning Projectiles. *J. Guid. Control* **1978**, *1* (2), 117–122.
3. D'Amico, W. Comparison of Theory and Experiment for Moments Induced by Loose Internal Parts. *J. Guid. Control* **1987**, *10* (1), 14–19.
4. Hodapp, A. Passive Means for Stabilizing Projectiles with Partially Restrained Internal Members. *J. Guid. Control* **1989**, *12* (2), 135–139.
5. Petsopoulos, T.; Regan, F.; Barlow, J. Moving Mass Roll Control System for Fixed-Trim Re-Entry Vehicle. *J. Spacecraft Rockets* **1996** *33* (1), 54–61.
6. Robinett, R.; Sturgis, B.; Kerr, S. Moving Mass Trim Control for Aerospace Vehicles. *J. Guid. Control Dynam.* **1996** *19* (5), 1064–1071.
7. Menon, P.; Sweriduk, G.; Ohlmeyer, E.; Malyevac, D. Integrated Guidance and Control of Moving Mass Actuated Kinetic Warheads. *J. Guid. Control Dynam*. **2004**, *27* (1), 118–127.
8. Frost, G.; Costello, M. Linear Theory of a Projectile with a Rotating Internal Part in Atmospheric Flight. *J. Guid. Control Dynam*. **2004**, *27* (5), 898–906.
9. Frost, G.; Costello, M. Control Authority of a Projectile Equipped With an Internal Unbalanced Part. *J. Dy. Syst. T ASME* **2006**, *128* (4), 1005–1012.
10. Rogers, J.; Costello, M. Control Authority of a Projectile Equipped with an Internal Translating Mass. *J. Guid. Control Dynam*. **2008**, *31*, (5), 1323–1333.
11. Slotine, J.; Li, W. ISBN 0-13-040890-5. *Applied Nonlinear Control*; Prentice Hall: New York, 1991, 207–236.
12. Purcell, E. ISBN 0-07-004908-4. *Electricity and Magnetism*; McGraw-Hill: New York, 1985, 227, 412-138.
13. Inman, D. ISBN 0-13-726-142-X. *Engineering Vibration*; Prentice Hall: New York, 2001, 451.

14. Flatau, A.; Dapino, M.; Calkins, F. High Bandwidth Tunability in a Smart Vibration Absorber. *J. Intell. Mat. Syst. Str.* **2000**, *11*, 923–929.

15. Varga, Z.; Filipcsei, G.; Zrinyi, M. Smart Composites with Controlled Anisotropy. *Polymer* **2005**, *46*, 7779–7787.

16. Varga, Z.; Filipcsei, G.; Zrinyi, M. Magnetic Field Sensitive Functional Elastomers With Tuneable Elastic Modulus. *Polymer* **2006**, *47*, 227–233.

17. Davis, C.; Lesieutre, G. An Actively Tuned Solid-State Vibration Absorber Using Capacitive Shunting of Piezoelectric Stiffness. *J. Sound Vib.* **2000**, *232* (3), 601–617.

Appendix A. *A* and *B* Matrix Terms

The terms of equation 22 are given as follows:

$$A_{11} = I_{T31} + BL\frac{m_P m_T}{m} s_\gamma r_3$$

$$A_{12} = I_{T32} - BL\frac{m_P m_T}{m} c_\gamma r_3$$

$$A_{13} = I_{T33} + BL^2\frac{m_P m_T}{m} + BL\frac{m_P m_T}{m}\left(c_\gamma r_2 - s_\gamma r_1\right)$$

$$A_{14} = I_{T33} + BL^2\frac{m_P m_T}{m}$$

$$A_{21} = I_{P31} - \frac{m_P m_T}{m} r_1 r_3$$

$$A_{22} = I_{P32} - \frac{m_P m_T}{m} r_2 r_3$$

$$A_{23} = I_{P33} + \frac{m_P m_T}{m} BL\left(r_2 c_\gamma - r_1 s_\gamma\right) + \frac{m_P m_T}{m}\left(r_1^2 + r_2^2\right)$$

$$A_{24} = \frac{m_P m_T}{m} BL\left(r_2 c_\gamma - r_1 s_\gamma\right)$$

$$A_{31} = I_{P21} + I_{T21} - \frac{m_P m_T}{m} BLr_4 c_\gamma - \frac{m_P m_T}{m} r_2 r_4$$

$$A_{32} = I_{P22} + I_{T22} - \frac{m_P m_T}{m} BLr_4 s_\gamma + \frac{m_P m_T}{m}\left(r_1 r_4 + r_3 r_6\right)$$

$$A_{33} = I_{P23} + I_{T23} - \frac{m_P m_T}{m} BLr_6 c_\gamma - \frac{m_P m_T}{m} r_2 r_6$$

$$A_{34} = I_{T23} - \frac{m_P m_T}{m} BLr_6 c_\gamma$$

$$A_{41} = I_{P11} + I_{T11} + \frac{m_P m_T}{m} BLr_5 c_\gamma + \frac{m_P m_T}{m}\left(r_2 r_5 + r_3 r_6\right)$$

$$A_{42} = I_{P12} + I_{T12} + \frac{m_P m_T}{m} BLr_5 s_\gamma - \frac{m_P m_T}{m} r_1 r_5$$

$$A_{43} = I_{P13} + I_{T13} + \frac{m_P m_T}{m} BLr_6 s_\gamma - \frac{m_P m_T}{m} r_1 r_6$$

$$A_{44} = I_{T13} + \frac{m_P m_T}{m} BLr_6 s_\gamma$$

$$B_1 = -\vec{K}_S \bullet \mathbb{S}\left(\vec{r}_{L\to X}\right) m_T \mathbb{C}_S\left(\vec{a}_{C/I}\right) - f_{Input} BLc_\gamma - k_T\gamma - k_D\dot{\gamma} - \vec{K}_S \bullet \mathbb{S}\left(\vec{\omega}_{B/I}\right) I_T \mathbb{C}_S\left(\vec{\omega}_{T/I}\right)$$
$$+\vec{K}_S \bullet \mathbb{S}\left(\vec{r}_{L\to X}\right)\mathbb{C}_S\left(\vec{W}_T\right) - \frac{m_P m_T}{m}\vec{K}_S \bullet \mathbb{S}\left(\vec{r}_{L\to X}\right)\mathbb{S}\left(\vec{\omega}_{T/I}\right)\mathbb{S}\left(\vec{\omega}_{T/I}\right)\mathbb{C}_T\left(\vec{r}_{L\to X}\right)$$
$$-\frac{m_P m_T}{m}\vec{K}_S \bullet \mathbb{S}\left(\vec{r}_{L\to X}\right)\mathbb{S}\left(\vec{\omega}_{B/I}\right)\mathbb{S}\left(\vec{\omega}_{B/I}\right)\mathbb{C}_S\left(\vec{r}_{P\to L}\right)$$
$$-\frac{m_P m_T}{m}\vec{K}_S \bullet \mathbb{S}\left(\vec{r}_{L\to X}\right)\left[\mathbb{S}\left(\vec{\omega}_{B/I}\right)\mathbb{C}_S\left(\vec{\omega}_{T/I}\right)\right]\times \mathbb{C}_S\left(\vec{r}_{L\to X}\right)$$
$$B_2 = -\vec{K}_S \bullet m_P \mathbb{S}\left(\vec{r}_{L\to P}\right)\mathbb{C}_S\left(\vec{a}_{C/I}\right) + f_{Input} BLc_\gamma + k_T\gamma + k_D\dot{\gamma} - \vec{K}_S \bullet \mathbb{S}\left(\vec{\omega}_{B/I}\right) I_P \mathbb{C}_S\left(\vec{\omega}_{B/I}\right)$$
$$+\vec{K}_S \bullet \mathbb{C}_S\left(\sum \vec{M}_P^L\right) + \frac{m_P m_T}{m}\vec{K}_S \bullet \mathbb{S}\left(\vec{r}_{L\to P}\right)\mathbb{S}\left(\vec{\omega}_{T/I}\right)\mathbb{S}\left(\vec{\omega}_{T/I}\right)\mathbb{C}_S\left(\vec{r}_{L\to X}\right)$$
$$+\frac{m_P m_T}{m}\vec{K}_S \bullet \mathbb{S}\left(\vec{r}_{L\to P}\right)\mathbb{S}\left(\vec{\omega}_{B/I}\right)\mathbb{S}\left(\vec{\omega}_{B/I}\right)\mathbb{C}_S\left(\vec{r}_{P\to L}\right)$$
$$+\frac{m_P m_T}{m}\vec{K}_S \bullet \mathbb{S}\left(\vec{r}_{L\to P}\right)\left[\mathbb{S}\left(\vec{\omega}_{B/I}\right)\mathbb{C}_S\left(\vec{\omega}_{T/I}\right)\right]\times \mathbb{C}_S\left(\vec{r}_{L\to X}\right)$$
$$+\vec{K}_S \bullet \mathbb{S}\left(\vec{r}_{L\to P}\right)\mathbb{C}_S\left(\vec{W}_P\right)$$
$$B_3 = -\vec{J}_S \bullet \mathbb{S}\left(\vec{\omega}_{B/I}\right) I_P \mathbb{C}_S\left(\vec{\omega}_{B/I}\right) - \vec{J}_S \bullet \mathbb{S}\left(\vec{\omega}_{T/I}\right) I_T \mathbb{C}_S\left(\vec{\omega}_{T/I}\right) + \vec{J}_S \bullet \mathbb{S}\left(\vec{r}_{L\to X}\right)\mathbb{C}_S\left(\vec{W}_T\right)$$
$$-\vec{J}_S \bullet m\mathbb{S}\left(\vec{r}_{L\to P}\right)\mathbb{C}_S\left(\vec{a}_{C/I}\right) - \vec{J}_S \bullet m_T \mathbb{S}\left(\vec{r}_{P\to X}\right)\mathbb{C}_S\left(\vec{a}_{C/I}\right)$$
$$-\frac{m_P m_T}{m}\vec{J}_S \bullet \mathbb{S}\left(\vec{r}_{P\to X}\right)\mathbb{S}\left(\vec{\omega}_{T/I}\right)\mathbb{S}\left(\vec{\omega}_{T/I}\right)\mathbb{C}_S\left(\vec{r}_{L\to X}\right)$$
$$-\frac{m_P m_T}{m}\vec{J}_S \bullet \mathbb{S}\left(\vec{r}_{P\to X}\right)\mathbb{S}\left(\vec{\omega}_{B/I}\right)\mathbb{S}\left(\vec{\omega}_{B/I}\right)\mathbb{C}_S\left(\vec{r}_{P\to L}\right) + \vec{J}_S \bullet \mathbb{C}_S\left(\sum \vec{M}_{system}^L\right)$$
$$-\frac{m_P m_T}{m}\vec{J}_S \bullet \mathbb{S}\left(\vec{r}_{P\to X}\right)\left[\mathbb{S}\left(\vec{\omega}_{B/I}\right)\mathbb{C}_S\left(\vec{\omega}_{T/I}\right)\right]\times \mathbb{C}_S\left(\vec{r}_{L\to X}\right)$$
$$B_4 = -\vec{I}_S \bullet \mathbb{S}\left(\vec{\omega}_{B/I}\right) I_P \mathbb{C}_S\left(\vec{\omega}_{B/I}\right) - \vec{I}_S \bullet \mathbb{S}\left(\vec{\omega}_{T/I}\right) I_T \mathbb{C}_S\left(\vec{\omega}_{T/I}\right) + \vec{I}_S \bullet \mathbb{S}\left(\vec{r}_{L\to X}\right)\mathbb{C}_S\left(\vec{W}_T\right)$$
$$-\vec{I}_S \bullet m\mathbb{S}\left(\vec{r}_{L\to P}\right)\mathbb{C}_S\left(\vec{a}_{C/I}\right) - \vec{I}_S \bullet m_T \mathbb{S}\left(\vec{r}_{P\to X}\right)\mathbb{C}_S\left(\vec{a}_{C/I}\right)$$
$$-\frac{m_P m_T}{m}\vec{I}_S \bullet \mathbb{S}\left(\vec{r}_{P\to X}\right)\mathbb{S}\left(\vec{\omega}_{T/I}\right)\mathbb{S}\left(\vec{\omega}_{T/I}\right)\mathbb{C}_S\left(\vec{r}_{L\to X}\right)$$
$$-\frac{m_P m_T}{m}\vec{I}_S \bullet \mathbb{S}\left(\vec{r}_{P\to X}\right)\mathbb{S}\left(\vec{\omega}_{B/I}\right)\mathbb{S}\left(\vec{\omega}_{B/I}\right)\mathbb{C}_S\left(\vec{r}_{P\to L}\right) + \vec{I}_S \bullet \mathbb{C}_S\left(\sum \vec{M}_{system}^L\right)$$
$$-\frac{m_P m_T}{m}\vec{I}_S \bullet \mathbb{S}\left(\vec{r}_{P\to X}\right)\left[\mathbb{S}\left(\vec{\omega}_{B/I}\right)\mathbb{C}_S\left(\vec{\omega}_{T/I}\right)\right]\times \mathbb{C}_S\left(\vec{r}_{L\to X}\right)$$

$$
\begin{aligned}
B_{FLC} = & -\vec{K}_S \bullet \mathbb{S}\left(\vec{r}_{L\to X}\right) m_T \mathbb{C}_S\left(\vec{a}_{C/I}\right) - k_T\gamma - k_D\dot{\gamma} - \vec{K}_S \bullet \mathbb{S}\left(\vec{\omega}_{B/I}\right) I_T \mathbb{C}_S\left(\vec{\omega}_{T/I}\right) \\
& + \vec{K}_S \bullet \mathbb{S}\left(\vec{r}_{L\to X}\right) \mathbb{C}_S\left(\vec{W}_T\right) - \frac{m_P m_T}{m} \vec{K}_S \bullet \mathbb{S}\left(\vec{r}_{L\to X}\right) \mathbb{S}\left(\vec{\omega}_{T/I}\right) \mathbb{S}\left(\vec{\omega}_{T/I}\right) \mathbb{C}_T\left(\vec{r}_{L\to X}\right) \\
& - \frac{m_P m_T}{m} \vec{K}_S \bullet \mathbb{S}\left(\vec{r}_{L\to X}\right) \mathbb{S}\left(\vec{\omega}_{B/I}\right) \mathbb{S}\left(\vec{\omega}_{B/I}\right) \mathbb{C}_S\left(\vec{r}_{P\to L}\right) \\
& - \frac{m_P m_T}{m} \vec{K}_S \bullet \mathbb{S}\left(\vec{r}_{L\to X}\right) \left[\mathbb{S}\left(\vec{\omega}_{B/I}\right) \mathbb{C}_S\left(\vec{\omega}_{T/I}\right)\right] \times \mathbb{C}_S\left(\vec{r}_{L\to X}\right)
\end{aligned}
$$

Appendix B. Translating Mass Projectile Schematic

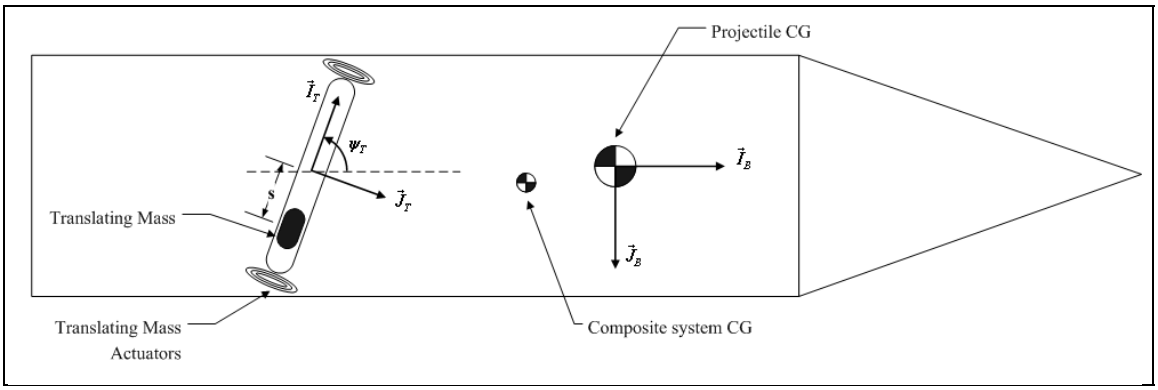

Figure B-1. Translating mass projectile schematic.

List of Symbols, Abbreviations, and Acronyms

$\boldsymbol{a}_1, \boldsymbol{a}_2, \boldsymbol{a}_3$	Components in the *S* frame of the acceleration of the system mass center with respect to the inertial frame
$\vec{\boldsymbol{a}}_{\boldsymbol{P/I}}$	Acceleration of the projectile mass center with respect to the inertial frame
$\vec{\boldsymbol{a}}_{\boldsymbol{X/I}}$	Acceleration of the end of the ITM-Beam with respect to the inertial frame
A	Maximum magnitude of ITM-Beam displacement from center of cavity
b	Radius of the electromagnetic actuator
BL	Length of the ITM-Beam assembly
$\vec{\boldsymbol{B}}_{\boldsymbol{z}}$	Magnetic field produced by the electromagnetic actuators in the $\vec{\boldsymbol{I}}_{\boldsymbol{S}}$ direction
C	Composite body center of mass
DM	Magnetic dipole moment of the fixed magnet at the end of the ITM-Beam
$\vec{F}_C$	Hinge constraint force on the internal translating mass
$\vec{F}_I$	Input force exerted by electromagnetic actuators on ITM-Beam
$\vec{F}_P$	Total aerodynamic force exerted on the projectile
$\boldsymbol{f}_{\boldsymbol{input}}$	Scalar value of the total force applied to ITM-Beam by electromagnetic actuators
$\vec{\boldsymbol{H}}^{\boldsymbol{P}}_{\boldsymbol{B/I}}$	Angular momentum of the projectile with respect to the inertial frame about the projectile center of mass
$\vec{\boldsymbol{H}}^{\boldsymbol{X}}_{\boldsymbol{T/I}}$	Angular momentum of the ITM-Beam with respect to the inertial frame about point *X*
$\boldsymbol{I}_{\boldsymbol{Txx}}$	The *xx* component of the ITM-Beam moment of inertia matrix about point *X*
$\boldsymbol{I}_{\boldsymbol{Pxx}}$	The *xx* component of the projectile moment of inertia matrix
$\vec{\boldsymbol{I}}_{\boldsymbol{I}}, \vec{\boldsymbol{J}}_{\boldsymbol{I}}, \vec{\boldsymbol{K}}_{\boldsymbol{I}}$	Inertial frame unit vectors
$\vec{\boldsymbol{I}}_{\boldsymbol{B}}, \vec{\boldsymbol{J}}_{\boldsymbol{B}}, \vec{\boldsymbol{K}}_{\boldsymbol{B}}$	Projectile reference frame unit vectors
$\vec{\boldsymbol{I}}_{\boldsymbol{N}}, \vec{\boldsymbol{J}}_{\boldsymbol{N}}, \vec{\boldsymbol{K}}_{\boldsymbol{N}}$	Nonrolling reference frame unit vectors

$\vec{I}_T, \vec{J}_T, \vec{K}_T$	ITM-Beam fixed frame unit vectors
$\vec{I}_S, \vec{J}_S, \vec{K}_S$	*S* frame unit vectors
I_E	Current through the electromagnetic actuator
k_D	Torsional damper coefficient
k_T	Torsional spring coefficient
L	Junction of between the ITM-Beam and the projectile, referred to as the "hinge point"
L_A	Length of the electromagnetic actuator
m_P	Mass of the projectile with the cavity
m_T	Mass of the ITM-Beam
m	Total mass of the system
$\vec{M}_P^L$	External moments applied to the projectile about the hinge point *L*
$\vec{M}_{system}^L$	External moments applied to the projectile-ITM system about the hinge point *L*
$\vec{M}_{Beam}^L$	External moment exerted on the ITM-Beam by the actuators in the $\vec{K}_S$ direction about the hinge point *L*
P	Projectile center of mass
$\vec{r}_{L\to X}$	Distance vector from the hinge point *L* to point *X* at the end of the ITM-Beam
$\vec{r}_{L\to P}$	Distance vector from the hinge point *L* to the projectile center of mass *P*
$\vec{r}_{P\to X}$	Distance vector from projectile center of mass *P* to point *X* at the end of the ITM-Beam
r_1, r_2, r_3	Components in the *S* frame of $\vec{r}_{P\to L}$
r_4, r_5, r_6	Components in the *S* frame of $\vec{r}_{P\to X}$
$\tilde{p}, \tilde{q}, \tilde{r}$	Components of $\vec{\omega}_{B/I}$ in the *S* frame
p, q, r	Components of $\vec{\omega}_{B/I}$ in the projectile reference frame

u, v, w	Translational velocity components of the composite body center of mass resolved in the projectile reference frame
$\vec{v}_{C/I}$	Velocity of the system mass center with respect to the inertial frame
$\vec{W}_P$	Weight of the projectile (without the ITM-Beam)
$\vec{W}_T$	Weight of the ITM-Beam
X	Point at the end of the ITM-Beam
x, y, z	Position vector components of the composite body center of mass expressed in the inertial reference frame
X_B, Y_B, Z_B	Total external force components on the projectile and ITM-Beam system expressed in the projectile reference frame
$\vec{\alpha}_{B/I}$	Angular acceleration of the projectile body with respect to the inertial frame
$\vec{\alpha}_{T/I}$	Angular acceleration of the ITM-Beam with respect to the inertial frame
γ	Deflection angle of the ITM-Beam
ϕ, θ, ψ	Euler roll, pitch, and yaw angles
θ_T, ψ_T	Euler pitch and yaw angles for the orientation of the *S* frame with respect to the *B* frame
$\vec{\omega}_{B/I}$	Angular velocity of the projectile body with respect to the inertial frame
$\vec{\omega}_{T/I}$	Angular velocity of the ITM-Beam with respect to the inertial frame
ω_{Beam}	Magnitude of the angular velocity of the ITM-Beam with respect to the *S* frame

NO. OF
COPIES ORGANIZATION

1 (PDF only) DEFENSE TECHNICAL INFORMATION CTR
DTIC OCA
8725 JOHN J KINGMAN RD
STE 0944
FORT BELVOIR VA 22060-6218

1 DIRECTOR
US ARMY RESEARCH LAB
IMNE ALC HRR
2800 POWDER MILL RD
ADELPHI MD 20783-1197

1 DIRECTOR
US ARMY RESEARCH LAB
RDRL CIM L
2800 POWDER MILL RD
ADELPHI MD 20783-1197

1 DIRECTOR
US ARMY RESEARCH LAB
RDRL CIM P
2800 POWDER MILL RD
ADELPHI MD 20783-1197

1 DIRECTOR
US ARMY RESEARCH LAB
RDRL D
2800 POWDER MILL RD
ADELPHI MD 20783-1197

ABERDEEN PROVING GROUND

1 DIR USARL
RDRL CIM G (BLDG 4600)

NO. OF COPIES	ORGANIZATION
4	GEORGIA TECH RSCH INST J MCMICHAEL K MASSEY A LOVAS M HEIGES 7220 RICHARDSON RD SMYRNA GA 30080
1	USAMCOM AMSAM RD MG J BAUMANN REDSTONE ARSENAL AL 35898-5000
1	USAMCOM AMSRD AMR SG SD B NOURSE REDSTONE ARSENAL AL 35898-5000
1	AFRL/MNGN G ABATE 101 W EGLIN BLVD STE 332 EGLIN AFB FL 32542
1	APPLIED PHYSICS LAB W DAMICO 11100 JOHNS HOPKINS RD LAUREL MD 20723-6099
1	GEORGIA TECH DANIEL GUGGENHEIM SCHOOL OF ARSPC ENGRG M COSTELLO 270 FERST DR ATLANTA GA 30332-0150
1	US AMRDEC AMSAM RD SS AT R KRETZSCHMAR BLDG 5400 REDSTONE ARSENAL AL 35898-5000
1	US RDECOM AMRDEC AMSRD AMR SG CT S DUNBAR BLDG 5400 REDSTONE ARSENAL AL 35898
1	US RDECOM AMSRD AMR SG SD J LOCKER BLDG 5400 REDSTONE ARSENAL AL 35898-5000

NO. OF COPIES	ORGANIZATION
4	COMMANDER ARDEC AMSRD AAR AEM L D OKKEN R BRYAN M HORVATH P BRISLIN BLDG 65S PICATINNY ARSENAL NJ 07806-5000
2	COMMANDER ARDEC AMSRD AAR AEM M LUCIANO M PALATHINGAL BLDG 65S PICATINNY ARSENAL NJ 07806-5000
2	COMMANDER ARDEC AMSRD AAR AEP E CHRIS STOUT D CARLUCCI BLDG 94 PICATINNY ARSENAL NJ 07806-5000
1	COMMANDER ARDEC AMSRD AAR AEM J G FLEMING BLDG 65N PICATINNY ARSENAL NJ 07806-5000
1	COMMANDER ARDEC AMSRD AAR AEM D G MOSHIER BLDG 65N PICATINNY ARSENAL NJ 07806-5000
1	COMMANDER ARDEC AMSRD AAR AIS SA D ERICSON BLDG 12 PICATINNY ARSENAL NJ 07806-5000
1	PROJECT MANAGER TANK MAIN ARMAMENT SYS SFAE GCSS TMA D GUZIEWICZ BLDG 354 PICATINNY ARSENAL NJ 07806-5000
1	APM SMALL & MEDIUM CALIBER AMMO OPM MAS SFAE GCSS TMA G DEROSA BLDG 354 PICATINNY ARSENAL NJ 07806-5000

NO. OF COPIES ORGANIZATION

1 COMMANDER
US ARMY TACOM ARDEC
SFAE GCSS MAS SMC
R KOWALSKI
BLDG 354
PICATINNY ARSENAL NJ 07806-5000

3 COMMANDER
US ARMY TACOM ARDEC
AMSTA AR FSP P
P MAGNOTTI
A LICHTENBER
G SCALON
BLDG 61S
PICATINNY ARSENAL NJ 07806-5000

1 COMMANDER
US ARMY TACOM ARDEC
AMSRD AAR
A MUSALLI
BLDG 65S
PICATINNY ARSENAL NJ 07806-5000

2 COMMANDER
US ARMY TACOM ARDEC
AMSRD AAR AEM L
G KOLASA
A MOUNA
BLDG 65S
PICATINNY ARSENAL NJ 07806-5000

11 US ARMY TACOM ARDEC
AMSRD AAR AEM A
G LIVECCHIA
J GRAU
G MALEJKO
E VAZQUEZ
W TOLEDO
L YEE
R TROHANOWSKY
S HAN
W KOENIG
S CHUNG
C WILSON
BLDG 95
PICATINNY ARSENAL NJ 07806-5000

1 COMMANDER
US ARMY TACOM ADRDEC
AMSRD AAR AEM L
R SAYER
BLDG 65
PICATINNY ARSENAL NJ 07806-5000

NO. OF COPIES ORGANIZATION

1 COMMANDER
US ARMY TACOM ADRDEC
SFAE AMO MAS LC
F CHANG
BLDG 65
PICATINNY ARSENAL NJ 07806-5000

1 COMMANDER
US ARMY TACOM ADRDEC
ATTN AMSTA AR CCH B
S PATEL
BLDG 65
PICATINNY ARSENAL NJ 07806-5000

1 COMMANDER
US ARMY TACOM
SFAE GCSS W AB QT
J MORAN
WARREN MI 48397-5000

2 COMMANDER
US ARMY TACOM
SFAE GCSS W
S COOPER
J NEFF
WARREN MI 48397-5000

1 COMMANDER
US ARMY TACOM
SFAE CSS TV
R GROLLER
WARREN MI 48397-5000

1 DIRECTOR
US ARMY ARMOR CTR
ATZK TS
W MEINSHAUSEN
FT KNOX KY 40121

1 SFSJM CDL
HQ US ARMY JOINT
MUNITIONS CMD AMSIO SMT
M RIVERS
1 ROCK ISLAND ARSENAL
ROCK ISLAND IL 61299-6000

2 DIRECTOR
BENET LAB
AMSTA AR CCB
J VASILAKIS
R HASENBEIN
WATERVLIET NY 12189

NO. OF
COPIES ORGANIZATION

ABERDEEN PROVING GROUND

35 DIR USARL
(1 CD) RDRL WML F
F BRANDON
S BUGGS
E BUKOWSKI
J CONDON
B DAVIS
R HALL
M HAMAOUI
T HARKINS
D HEPNER
K HUBBARD
M ILG
G KATULKA
D LYON
J MALEY
D MCGEE
C MILLER
P MULLER
P PEREGINO
B TOPPER
RDRL WML
J NEWILL
M ZOLTOSKI
RDRL WML E
V BHAGWANDIN
I CELMINS
G COOPER
J DESPIRITO
L FAIRFAX
F FRESCONI
J GARNER
B GUIDOS
K HEAVEY
B HOWELL
G OBERLIN
J SAHU
S SILTON
P WEINACHT (1 CD)

INTENTIONALLY LEFT BLANK.